Braiding Braak and Braak:

Staging patterns and model selection in network neurodegeneration

Prama Putra, Travis Thompson*, and Alain Goriely

Mathematical Institute, University of Oxford

February 2, 2021

Abstract

A hallmark of Alzheimer's disease is the aggregation of insoluble amyloid-beta plaques and tau protein neurofibrillary tangles. A key histopathological observation is that tau protein aggregates follow a clear progression pattern through the brain; characterized by six distinct stages. This so-called 'Braak staging pattern' has become the gold standard for Alzheimer's disease progression. It has also been suggested, via a histopathological analysis, that soluble seed-competent tau seeding precedes tau aggregation in the same manner. Mathematical models such as prion-like propagation on networks have the ability to capture key feature of the dynamics. Here, we study the staging of tau proteins using a model of proteopathy that include both local growth due to autocatalytic effects and diffusion along axonal pathways. We develop new methods to capture the staging patterns and use these as a qualitative criterion to identify the best model for diffusion process on networks and to identify possible parameter regimes. Our analysis provides a systematic way to study Braak staging in neurodegenerative processes.

1 Introduction

The term 'neurodegenerative disease' refers to a family of maladies primarily affecting the brain's neurons; many neurodegenerative diseases result in cognitive decline and, ultimately, a diagnosis of dementia. A hallmark of such diseases is a large concentration of toxic protein aggregates throughout the brain. These toxic proteins interfere with normal brain functions and are associated with neuronal impairment, neuronal loss, brain atrophy, and overall cognitive decline. In this manuscript we address an important facet of the most contemporarily prevalent cause of dementia; Alzheimer's disease (AD). The practical constraints of clinical AD experiments in humans have lead to a flurry of interest around the development of mathematical and computational models of pathology evolution; particularly those that can accurately capture large-scale features of the disease. Many of these models take advantage of the prion hypothesis which asserts that the progression of proteopathy, in AD, follows from a prion-like mechanism.

*Corresponding author, travis.thompson@maths.ox.ac.uk

Prion-like mathematical, or computational, models can be broadly characterized as either probabilistic models [1, 2, 3] or as continuous, nonlinear, transversely anisotropic, reaction-diffusion systems [4, 5, 6, 7, 8, 9, 10, 11, 12, 13, 14]; they are then either discretized, and solved, on a simplicial mesh [4, 5, 6], or on the network defined by the brain's connectome [7, 8, 9, 10, 11, 12, 13, 14]. Diffusion-reaction models of proteopathy discretized on a structural connectome have some advantages over their simplicial counterparts. First, diffusive transport orthogonal to white-matter bundles is thought to be quite small in comparison with the axonal direction and, thus, the traditional resolution advantage of simplicial discretizations are obviated in the absence of additional coupled, multiphysics processes; second, network discretization of diffusion-reaction systems provides a coupled non-linear system of ordinary differential equations for which tools from dynamical systems can be readily applied; third, fast solvers for stiff non-linear ordinary differential equation systems are readily available and easy to work with; and fourth, network models, even for connectomes with thousands of nodes and tens of thousands of edges, can be solved several orders of magnitude faster than simplicially discretized models.

It is well-known that the appearance of tau protein (τP) aggregates follow a regional progression codified by distinct stages [15, 16] and recent evidence suggests this also holds true for seed-competent soluble τP [17]. Despite the notable contemporary interest in network models of proteopathy, and their computational advantages, little has been done to investigate the question of τP anatomical staging for these models. Here, we study in detail Braak staging patterns for τP seeding [17] and histopathological neurofibrillary tangles (NFT) pathology [15, 16] using a nonlinear reaction-diffusion model based on the Fisher-Kolmogorov-Petrovsky-Piskunov (Fisher-KPP) equation discretized on the structural white-matter connectome. The primary results of are threefold. First, we show that among the possible choices for diffusion processes on a network, the classical graph Laplacian is the only robust choice which preserves mass conservation and Fick's law. Second, we show that the choice of connectome has a strong influence on the staging pattern and that low-resolution connectome are not adequate to capture the correct staging pattern. Third, we identify parameter regimes consistent with the Braak pattern. Together, these results offer a systematic method to identify the best possible model (model selection), and identify the best possible parameter regimes (model identifiability), in order to match a known staging outcome for a neurodegenerative disease propagation process over a connectome network.

2 Preliminaries

First, we introduce the staging of τP using a network-based model, we briefly summarize τP staging and outline the construction of a structural brain connectome from patient imaging data. Then, we develop a method based on braid diagrams for visualizing complex staging patterns.

2.1 A brief overview of AD proteopathy and tau staging

A hallmark of AD, and many other neurodegenerative diseases, is the replication and spreading of toxic, misfolded proteins within the brain; Amyloid-beta (Aβ) and tau protein in the case of AD. In particular, AD is classified primarily by the presence of toxic Aβ protein plaques and toxic τP NFT or neuropil threads. According to the prion-like hypothesis [18, 19, 20, 21, 22, 23], the formation of insoluble Aβ plaques and τP NFT follow a similar, high-level pattern: healthy Aβ and τP monomers become misfolded; the misfolded template spread the characteristic to other proteins;

misfolding induces aggregation into fibrils; these intermediate structures aggregate together to form plaques and NFT. Misfolded proteins induce various types of extra- and intra-cellular 'toxic' effects on neurons and their surrounding tissue environment [24, 25, 26, 27, 28, 29]; both separately and through joint interaction [30, 31, 32, 14]; leading, eventually, to dementia.

AD pathology is complex. Despite the nuances underlying the toxic tango of interacting τP and Aβ proteins, one biomarker remains a consistent indicator of disease progression; the staging characteristics of τP NFT pathology. The staging patterns of NFT pathology were first codified by Braak and Braak [15]; NFT staging in AD is consistently stepwise, ordered and hierarchical in nature. It was suggested by Braak and Braak that AD-associated tau NFT progression manifests in six distinct stages. These stages, termed the 'Braak Stages' of AD pathology, can be generalized into three categorical units [15, 33, 16]: the transentorhinal stages (stage I-II); the limbic stages (stage III-IV); and the isocortical stages (stage V-VI). Ascertaining a patient's Braak stage is typically carried out post mortem; ruling out the viability of a certifiable assessment as a diagnostic tool. A recent post-mortem study [17] suggests that soluble seed-competent τP precedes the presence of overt τP NFT pathology. In particular, seed-competent τP (also referred to as τP seeds) develop along the Braak pathway in the same step-wise manner; thus offering further support to the prion-like hypothesis, and suggesting that simple models of toxic τP seed propagation may be augmented by an equation describing a subsequent aggregation process to form NFT tangles.

2.2 The structural connectome brain network

The *connectome* is a network whose nodes correspond to physical regions of the brain; two nodes are connected if they are associated in a particular way. Broadly speaking, the type of association used to justify the connection of two nodes determines the type of connectome produced. For example, one might look at the strength of the correlation between the neural activity in two regions of the brain while a patient lies at rest in a scanner. If the correlation between two regions meets a particular threshold then one would consider the corresponding nodes to be connected and, if desired, with a weight reflecting the correlation strength; leading to a so-called 'functional connectome' [34, 35, 36].

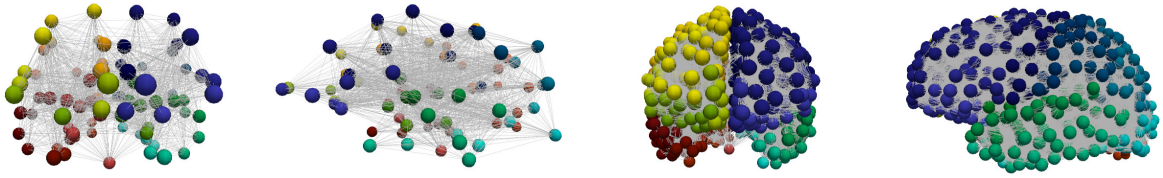

(a) Scale-33 Coronal (b) Scale-33 Sagittal (c) Scale-500 Coronal (d) Scale-500 Sagittal

Figure 1: Lowest (left) and highest (right) resolution patient structural connectomes with 83 and 1015 nodes, respectively. Nodes are assigned their color based on their classification into 83 disjoint anatomical region of interests.

Another common connectome to consider is the structural connectome [36, 37] encoding axonal pathways between regions. To generate such a connectome, a patient first receives a set of diffusion weighted MRI (dMRI) scans; these scans provides information about the local movement of water molecules within the brain. Then, the patient undergoes a T1 weighted MRI scan; this scan provides structural information that can be used, alongside an atlas-based segmentation al-

gorithm, to identify brain regions of interest. The flow patterns of water molecules in the brain, derived from the dMRI scans, are highly anisotropic due to the axonal bundles of the brain's white matter. The diffusion tensor, a 3×3 matrix with spatially varying entries that codifies the flow directions of these water molecules, is also inferred from the dMRI scan. The axonal fibers are then approximately reconstructed, from the local diffusion tensor information, using a deterministic or probabilistic streamline algorithm [34, 35, 38]. Finally, the segmented T1 image and the results of the tractographic reconstruction can be co-registered [36, 37] to create a connectivity matrix which, in turn, can be represented as a network. The nodes of the network correspond to the regions of the atlas used in the segmentation, and the edges of the network represent an approximation of the axonal fiber tractography data connecting those regions (c.f. Fig. 1) (see [36, 37] for details).

Here, we examine staging in a set of undirected, multi-resolution structural connectomes derived from 426 patient subjects [39] participating in the Human Connectome Project (c.f. Supplementary Data). This set of connectome data is presented, for each patient, at five resolutions [37]; each resolution has the same overall set of 83 general regions of interest but regions of interest are further subdivided as resolution increases. The lowest resolution connectome (Scale-33), Fig. 1a and Fig. 1b, consists of 83 nodes, one for each cortical or subcortical region of interest, and 1,654 axonal edges; the highest resolution network (Scale-500), Fig. 1c and Fig. 1d, consists of 1015 nodes, over the 83 regions of interest, and 70,892 axonal edges. The intermediate resolutions are: the Scale-60 connectome, with 129 nodes and 3,472 edges; the Scale-125 connectome, with 234 nodes and 9,217 edges; and the Scale-250 connectome, with 463 nodes and 25,023 edges. Tractography for the connectomes [39] consists of determining fibers, or streamlines, using High Angular Resolution Diffusion Images (HARDI) alongside constrained spherical deconvolution and probabilistic streamline tracking [40] methods to determine fiber orientation and tracking reconstruction. Individual streamlines are then grouped into bundles based on connectivity to a multi-resolution set of region of interest [36, 37] parcellations (ROIs). As is standard, edges between the node ROIs represent a collection of fiber streamlines; both the number of fibers (n_{ij}), and the mean fiber length (ℓ_{ij}), are available for each edge in the dataset [39]; the mean fiber length is reported in units of millimeters.

3 A connectome diffusion-reaction model of τP proteopathy

Many authors have now considered the propagation of protein pathology within the brain using mathematical models. These models range from complex, probabilistic [1, 41] network models, fitted to substantial amounts of patient data, to deterministic, non-linear models of reaction-diffusion type. These reaction-diffusion models are defined continuously [5, 42] and on structural brain connectomes [8, 12, 13, 14]. They offer a differential-equations-based framework for a data-independent analysis of disease characteristics.

In this section we briefly describe a general form of a single-species diffusion-reaction model, and discuss the connection to brain modeling vis-a-vis the prion-like hypothesis and clearance mechanisms for misfolded proteins in the brain. We then specialize the model to the so-called Fisher-KPP equation and briefly overview the discretization on networks using the graph Laplacian; finally, we state the expected properties that the graph Laplacian should satisfy in order to be consistent with the continuous case.

3.1 A continuous diffusion-reaction model

Our focus here is on non-linear reaction-diffusion models. The typical scalar is form for such models is

$$\frac{\partial p}{\partial t} = \rho \nabla \cdot (\mathbf{K} \nabla p) + R(p), \tag{1}$$

where p is the concentration of misfolded τP, $R(p)$ represents the non-linear reaction term for the model, $\mathbf{K}$ is a (symmetric) matrix diffusion tensor and ρ is an effective diffusion constant; when the diffusion is isotropic, $\mathbf{K}$ is a multiple of the identity matrix and $\nabla \cdot (\mathbf{K} \nabla p) = \rho \Delta p$ is the usual continuous Laplacian operator. In the brain, axonal white-matter bundles heavily bias the diffusion of extracellular fluid; leading to a transversely anisotropic diffusion tensor [5] with general form

$$\mathbf{K} = d_{\perp} \mathbf{I} + \left(d_{||} - d_{\perp}\right) \gamma \otimes \gamma, \tag{2}$$

where $\mathbf{I}$ is the identity matrix, $d_{\perp} \ll d_{||}$ and γ is a unit vector oriented along the fiber bundle. We now note two properties of (1). First, the form of the diffusive term, $\nabla \cdot (\mathbf{K} \nabla p)$, in (1) is a direct result of Fick's law of diffusion. Second, in the absence of clearance mechanism or reaction, the diffusive process conserves mass. Both feature should be conserved in a discretized version of the problem.

Here, we will study the Braak staging behavior, on networks, of the simplest, single-species model for the prion-like propagation of τP proteopathy presented in previous literature [5, 6, 12]; the Fisher-Kolmogorov-Petrovsky-Piskunov (Fisher-KPP) model. This model allows for a direct study of staging in the presence of prion-like growth (due to the reaction terms) and diffusive transport (due to the diffusion operator). The Fisher-KPP model is defined by setting and $R(p) = \alpha p(1-p)$ to obtain

$$\frac{\partial p}{\partial t} = \rho \nabla \cdot (\mathbf{K} \nabla p) + \alpha p(1-p), \tag{3a}$$

$$p(x, 0) = p_0(x), \tag{3b}$$

$$K \nabla p \cdot n = 0 \quad \text{on } \partial\Omega, \tag{3c}$$

where $0 \leq \alpha$ determines the local growth rate, potentially varying smoothly in space, and $p_0(x)$ is the initial seeding of τP. We will be particularly interested in the Braak staging behavior of network discretizations of (3) with respect to the relative size of the parameters ρ and α; the Fisher-KPP model has two asymptotic regimes:

Diffusion-dominated	$\max_{\Omega} \alpha \ll \rho$,
Growth-dominated	$\rho \ll \min_{\Omega} \alpha$.

3.2 Connectome discretizations of diffusion-reaction models

The problem now is to find the best discretizations of the spreading process by using the network structure of the brain. While some mouse models are sufficiently precise to establish directionality and hence build a directed connectome [2, 43], there is no clear evidence or data to support the claim that the human brain connectome induces directed flow. Moreover, there is no available directional human structural connectome and it has been shown theoretically that directionality has very little appreciable impact on the overall spreading dynamics [44].

Therefore, for the rest of this paper, we use an undirected connected network $G = (V, E)$ with $|V| = N \geq 3$ nodes and $|E| = M \geq 2$ edges. We further assume that the network is weighted with positive weight $W_{ij} = W_{ji}$ at an edge joining node i to node j. The weight is zero if two nodes are not connected, strictly positive if two nodes are connected, and such that $W_{ii} = 0$ (i.e there is no edge connecting a node to itself). Therefore, the weights define the $N \times N$ symmetric *weighted adjacency matrix* $\mathbf{W}$ with entries W_{ij}.

Since the diffusion tensor is primarily directed along the axonal fiber bundles, it is natural to consider propagation along edges constructed from fiber tractography. To do so, we replace scalar fields, such as p, $\partial_t p$, $\alpha(x)$ etc, with regional (node) averages, denoted by p_i, $\dot{p}_i$, or α_i etc, and replace the continuous diffusion operator $\nabla \cdot (\mathbf{K} \nabla p)$ with a graph Laplacian. This type of discretization strategy can be considered as motivated by, for instance, finite volume methods [45, 46] applied, in space, to (1) with a simple quadrature, such as the midpoint rule, for estimating the (spatial) integral of the non-linear term, $R(p)$, on a mesh whose cell faces are constructed orthogonal to the fiber directions. A natural discretization of (1) is

$$\frac{\mathrm{d}p_i}{\mathrm{d}t} = -\sum_{j=1}^{N} \mathcal{L}_{ij} p_j + R(p_i), \tag{4}$$

where p_i is the concentration at each node i and $\mathcal{L}$ is a graph Laplacian, a $N \times N$ matrix characterizing diffusion on the connectome. Note that the minus sign in front of $\mathcal{L}$ is just a matter of convention and has no particular significance).

3.3 Many graph Laplacians

The first problem, before we investigate the dynamics, is to decide which graph Laplacian to use. We need to use a Laplacian that models diffusion processes while respecting fundamental physical principles. The problem can be decomposed into two questions: what is the form of the graph Laplacian to use for a given weighted adjacency matrix? and what is the best choice of weights? To answer these question, we first consider a purely diffusive process:

$$\frac{\mathrm{d}\mathbf{p}}{\mathrm{d}t} = -\mathcal{L} \cdot \mathbf{p}, \tag{5}$$

where $\mathbf{p} = (p_1, \ldots, p_n)$ is the (column) vector of concentrations.

In the absence of sinks or sources, a diffusion process is mass conserving. If we assume in the first instance that each node has the same volume, then the total mass of the system is conserved. Therefore, the mass conservation condition (C1) imposes that

$$\sum_{i=1}^{n} \frac{\mathrm{d}p_i}{\mathrm{d}t} \equiv \mathbf{1} \cdot \frac{\mathrm{d}\mathbf{p}}{\mathrm{d}t} = 0, \tag{6}$$

where $\mathbf{1} = (1, \ldots, 1)$ is the one vector. Using (5), this condition implies

$$\mathbf{1} \cdot \mathcal{L} \cdot \mathbf{p} = 0, \tag{7}$$

which must be true for all $\mathbf{p}$. Hence we have the condition

$$\text{(C1)} \quad \mathbf{1} \cdot \mathcal{L} = \mathbf{0}, \tag{8}$$

where $\mathbf{0} = (0, \ldots, 0)$ is the null vector. In other words, the one vector is in the Laplacian's left nullspace. The existence of at least one zero eigenvalue for $\mathcal{L}$ implies that the right nullspace is non-empty. Hence, there exists a vector $\widehat{\mathbf{c}}$ such that

$$\mathcal{L} \cdot \widehat{\mathbf{p}} = \mathbf{0}, \tag{9}$$

which defines a steady-state concentration.

If $\mathcal{L} = \mathcal{L}^T$ we must have $\widehat{\mathbf{p}} = \mathbf{1}$. This condition is related to the Fick's condition (C2) that in the absence of a concentration gradient, there is no diffusion flux. The general form of this condition is that if all concentrations are equal, there is no change in concentration. Hence, for general undirected networks, we must have

$$\text{(C2)} \quad \mathcal{L} \cdot \mathbf{1} = \mathbf{0}. \tag{10}$$

In addition, we impose (C3) a *robustness condition:* C1 and C2 should hold for all connected undirected networks $G = (V, E)$. Indeed, there is no preferred atlas for segmenting the brain, and the choice of atlas impacts every downstream attribute of the connectomes [38, 47, 48, 49]; thus, variations in W_{ij} should not lead to the loss of the fundamental physical principles reflected by C1 and C2. Finally, the exact dependence of the flow characteristics, and thus on $\mathbf{W}$ and hence $\mathcal{L}$, due to fiber bundle attributes is not known; in the absence of this specific knowledge, the physics of a suitable graph Laplacian should be robust to variations in $\mathbf{W}$.

The standard graph Laplacian The *standard graph Laplacian* for an undirected network with weighted adjacency matrix $\mathbf{W}$ is

$$\mathbf{L} = \mathbf{D} - \mathbf{W}. \tag{11}$$

where $\mathbf{D} = \text{diag}(\mathbf{d})$ is the degree matrix, a diagonal matrix with diagonal entries $\mathbf{d} = \mathbf{W} \cdot \mathbf{1}$, the vector of nodal degrees. If $\mathbf{W}$ is Boolean (i.e. with entries 1 or 0), the degree is the number of edges arriving at each node (e.g. if $d_1 = 2$, the first node has two edges connecting other nodes).

A family of Laplacians While the standard graph Laplacians is often used in many physical applications [12, 13, 14], various other forms have been studied in the literature [7, 9, 8]. For instance, in the early use of network diffusion to model proteopathy in neurodegenerative disease [7, 9] the normalized form graph Laplacian is used. The same model has been used to study the relationship between structural and functional connectivity [9], atrophy in Alzheimer's disease [8], and pathology in both supranuclear palsy [10], and Parkinson's disease [50]. The *normalized graph Laplacian* used in these works is

$$\mathbf{L}_{1/2,1/2} = \mathbf{I} - \mathbf{D}^{-1/2}\mathbf{W}\mathbf{D}^{-1/2}. \tag{12}$$

Other possible Laplacian matrices can be defined and have been used in various studies such as spectral clustering, including

$$\mathbf{L}_{1,0} = \mathbf{I} - \mathbf{D}^{-1}\mathbf{W} = \mathbf{D}^{-1}\mathbf{L}, \tag{13}$$

$$\mathbf{L}_{0,1} = \mathbf{I} - \mathbf{W}\mathbf{D}^{-1} = \mathbf{L}\mathbf{D}^{-1}, \tag{14}$$

which motivates the introduction of the family

$$\mathbf{L}_{a,b} = \mathbf{D}^{1-a-b} - \mathbf{D}^{-a}\mathbf{W}\mathbf{D}^{-b} = \mathbf{D}^{-a}\mathbf{L}\mathbf{D}^{-b}, \tag{15}$$

with $a, b \in [0,1]$ and $a+b \leq 1$. We have $\mathbf{L} = \mathbf{L}_{0,0}$ and we note that since the network is connected, the degree of each node is strictly positive and the inverse of $\mathbf{D}$ is therefore defined. We can now state the main result of this section

Proposition 1. *Suppose $G = (V, E)$ is a connected undirected network with weighted adjacency matrix $\mathbf{W}$. Then, the standard graph Laplacian $\mathbf{L}_{0,0} = \mathbf{L}$ is the only member of the family* (15) *that satisfies conditions C1–C3.*

Proof. From the identities

$$\mathbf{D} \cdot \mathbf{1} = \mathbf{1} \cdot \mathbf{D} = \mathbf{W} \cdot \mathbf{1} = \mathbf{1} \cdot \mathbf{W} = \mathbf{d}, \tag{16}$$

It follows that

$$\mathbf{L} \cdot \mathbf{1} = \mathbf{1} \cdot \mathbf{L} = \mathbf{0}. \tag{17}$$

Hence the standard Laplacian $\mathbf{L}$ satisfies conditions C1-C2. Condition C3 is satisfied by the fact that these relationships do not depend on the form of $\mathbf{W}$. Hence, changes in the weight will not affect either condition.

Next, we show that $\mathbf{L}_{0,0}$ is the only member of the family (15) satisfying C1–C3. Let $a, b \in [0,1]$, with $a+b \leq 1$, be arbitrary but fixed with at least one of $a > 0$ or $b > 0$. First, consider conditions C2 and C3. From (15), and C2 we have

$$\mathbf{L}_{a,b} \cdot \mathbf{1} = \mathbf{D}^{1-a-b} \cdot \mathbf{1} - \mathbf{D}^{-a}\mathbf{W}\mathbf{D}^{-b} \cdot \mathbf{1} = \mathbf{0}.$$

The ith component of the above equation is

$$d_i^{1-a-b} - \sum_{j=1}^{N} \frac{W_{ij}}{d_i^a d_j^b} = \frac{d_i}{d_i^a d_i^b} - \sum_{j=1}^{N} \frac{W_{ij}}{d_i^a d_j^b} = 0.$$

Multiplying through by d_i^a and using the definition of $\mathbf{D}$ in terms of $\mathbf{W}$ yield

$$\sum_{j=1}^{N} \left(\frac{W_{ij}}{d_i^b} - \frac{W_{ij}}{d_j^b} \right) = \sum_{j=1}^{N} \frac{W_{ij}(d_j^b - d_i^b)}{d_j^b d_i^b} = 0. \tag{18}$$

Since this identity must be respected for all undirected connected graphs (condition C3), it must be independent of $\mathbf{W}$, hence we must have

$$d_j^b - d_i^b = 0, \tag{19}$$

for all pairs (i, j). This condition is satisfied by either $b = 0$ or $d_i = d_j$. If $d_i = d_j$ for all nodes and since there are at least 3 nodes in the network, one can change the weight of a single edge connected to one of the node, say i, but not the other by adding an arbitrarily small amount $0 < \epsilon \ll 1$ to that weight, with the effect of changing d_i but not d_j. Hence, the equality $d_i = d_j$ cannot hold under the robustness assumption and we conclude that $b = 0$ is the only condition for which C2 and C3 hold simultaneously.

Next we consider the conditions C1 and C3. From (15), and C1 we have

$$\mathbf{1} \cdot \mathbf{L}_{a,b} = \mathbf{1} \cdot \mathbf{D}^{1-a-b} - \mathbf{1} \cdot \left(\mathbf{D}^{-a}\mathbf{W}\mathbf{D}^{-b} \right) = \mathbf{0}.$$

The jth component of the column vector corresponding to the above equation states that

$$d_j^{1-a-b} - \sum_{i=1}^{N} \frac{w_{ij}}{d_j^a d_i^b} = \frac{d_j}{d_j^a d_j^b} - \sum_{i=1}^{N} \frac{w_{ij}}{d_i^a d_j^b} = 0,$$

must hold identically. Multiplying through by the common term d_j^b and using the symmetry of the adjacency matrix yield

$$\sum_{i=1}^{N} \left(\frac{W_{ij}}{d_j^a} - \frac{W_{ij}}{d_i^a} \right) = \sum_{i=1}^{N} \frac{W_{ij}(d_i^a - d_j^a)}{d_j^a d_i^a} = 0. \tag{20}$$

As in the previous case, the robustness condition C3 implies that

$$d_i^a - d_j^a = 0, \tag{21}$$

for all pairs (i, j) and we conclude that mass conservation and robustness imply that $a = 0$. Taken together conditions C1, C2, C3 imply that $a = b = 0$ must follow. □

To conclude, when we model the diffusion of a physical substance on a network, one must ensure that general physical principles are satisfied. We showed here that within the family of graph Laplacians that have been proposed, the only possible choice is the standard graph Laplacian. Therefore, we chose

$$\mathcal{L} = \rho \mathbf{L}, \tag{22}$$

where ρ is a scalar introduced for convenience and weight scaling purpose (see below). Any other choice of Laplacian will lead to a dynamics that either does not conserve total mass in the absence of sinks and sources or create a flux when all concentrations are equal.

3.4 Correction for varying volumes

If the nodes have different volumes $\boldsymbol{\nu} = (\nu_1, \ldots, \nu_n)$, then the condition for the conservation of mass C1 has to be modified. Indeed the total mass is now $P = \boldsymbol{\nu} \cdot \mathbf{p}$. Enforcing $\dot{P} = 0$ in (5), implies

$$\boldsymbol{\nu} \cdot \mathcal{L} = \mathbf{0}. \tag{23}$$

This condition can easily be achieved by choosing

$$\mathcal{L} = \rho \mathbf{L}_V = \rho \nu \mathbf{V}^{-1} \mathbf{L}, \tag{24}$$

where $\mathbf{V} = \text{diag}(\boldsymbol{\nu})$ and ν is a characteristic volume (average volume for instance). We note that this modified graph Laplacian is not symmetric, but that Fick's condition is still satisfied ($\mathbf{L}_V \cdot \mathbf{1} = \mathbf{0}$) since diffusion takes place when a concentration gradient is established, independently of the nodes' volume. We also note that the multiplication of the standard Laplacian on the left by a diagonal matrix has been used to define regions of vulnerability [43, 2], hence assuming that diffusion takes place differently in different nodes. Mathematically, it is the same operation but its interpretation in term of volumes or vulnerability is different and corresponds to different modeling choices (i.e. if we insist on mass conservation then mass should be conserved and interpreting $\mathbf{V}^{-1}$ as vulnerability precludes mass conservation).

3.5 Weight selection for the graph Laplacian

We have shown that for a given weighted adjacency matrix, the standard Laplacian (or its generalization for volume correction) is suitable to model diffusion. The modeling question is then to identify the best choice for the weights on the edge. The weighted adjacency matrix is determined by the connectivity of the axonal fibers in addition to measured attributes for the fiber bundle. A primary hypothesis of this manuscript is that the diffusive characteristics along a bundle are influenced by both the number n_{ij} of fibers in the bundle and its mean length ($\ell_{ij} > 0$, available as part of the connectome data. For the parameters n_{ij}, several studies (see [51] and the sources cited therein) have pointed out the influence of myelination on perturbing the flow patterns. More specifically, demyelination leads to a strengthening of radial diffusivity and thus a less directed cerebral water flow. Thus, we make the simplified modeling hypothesis that increased myelin density, reflected through higher values of n_{ij} along a fiber, increases the propensity of diffusion over that edge. A simple modeling of this principle is to take W_{ij} proportional to n_{ij} (and $W_{ij} = 0$ in the absence of a connection corresponding to $n_{ij} = 0$. We also consider the hypothesis that diffusive flux either remains constant or decreases as ℓ_{ij} increases. We consider simple models for this effect where the entries of $\mathbf{W}$, take one of the three forms for a node i connected to a node j,

$$\text{Length-free:} \qquad W_{ij} = n_{ij}, \tag{25a}$$

$$\text{Ballistic:} \qquad W_{ij} = \frac{n_{ij}}{\ell_{ij}}, \tag{25b}$$

$$\text{Diffusive:} \qquad W_{ij} = \frac{n_{ij}}{\ell_{ij}^2}, \tag{25c}$$

where, for definiteness, we take $\ell_{ij} = 1$ if $n_{ij} = 0$. In addition, we recall that $W_{ii} = 0$ per assumption and that $W_{ij} = W_{ji}$ as the network is undirected.

The choice (25a) was used in diffusion models of proteopathy [7, 9, 8], whereas (25b) has been used in the context of more complex reaction and aggregation models [12, 13] and (25c) appeared first in a model of Aβ-τP interaction in Alzheimer's disease [14]. Since the dimensional Laplacian $\mathcal{L} = \rho\mathbf{L}$ has unit of 1/time, the constant ρ has either units of 1/time for the length-free scaling (25a), length over time, i.e. units of velocity for the choice (25b) or length-squared over time, i.e. the units of diffusivity for (25c). Furthermore, the graph Laplacian scheme resulting from (25c) is identical to a conservative finite volume method [45, 46] when the network $G = (V, E)$ is a lattice. Thus, this choice of weights is a generalization of well-known conservative numerical flux discretizations.

4 The staging problem: braiding diagrams

In this section we introduce the *staging problem* for a dynamical system defined on a network $G = (E, V)$ with edge set E and node set V. We will introduce *braid diagrams* as a means of investigating the staging problem visually. Both the staging problem and braid diagrams can be formulated for a general dynamical system, defined on a given network, having the general form

$$\dot{\mathbf{p}}(t) = f(t, \mathbf{p}), \tag{26a}$$

$$\mathbf{p}(0) = \mathbf{p}_0, \tag{26b}$$

where $\mathbf{p}_i(t)$ denotes a normalized and dimensionless quantity, e.g. a normalized concentration $0 \leq \mathbf{p}_i(t) \leq 1$, corresponding to each network node $v_i \in V$. Here, we refer to the initial value, $\mathbf{p}(0)$, as a *seeding* in analogy with misfolded toxic oligomer 'seeds' in the study of neurodegenerative disease; we also refer to the nodes (or a collection of nodes) as 'regions of interest' (ROIs) in analogy with regional atlas labels used in brain imaging studies. For the remainder of the paper we will be concerned with a specific instance of (26) given by a graph discretization of (3). This system has the form

$$\frac{\mathrm{d}p_i}{\mathrm{d}t} = -\rho \sum_{j=1}^{N} L_{ij} p_j + \alpha p_i (1 - p_i), \tag{27a}$$

$$p_i(0) = p_{i,0}, \quad i = 1, 2, \ldots, N, \tag{27b}$$

where each of the initial values $p_{i,0}$ satisfy $0 \leq p_{i,0} \leq 1$. The Neumann boundary condition (3c) enforces mass conservation for the continuous model (3); in our case, this condition is enforced, for all possible weightings, by the choice of graph Laplacian (15) with $a = b = 0$. Given a dynamical system on a network, e.g. (27), an initial seeding, and a set of prescribed concentration thresholds, the *staging problem* is: to determine an ordering of the ROIs, for each threshold value, which reflects the order in which the ROIs achieved that value.

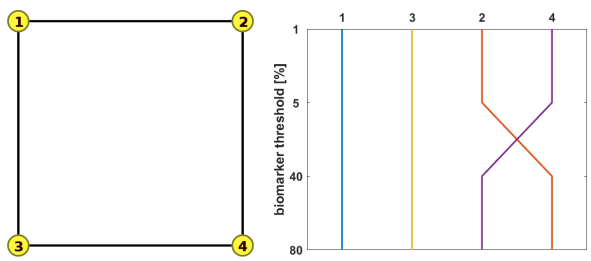

(a) A network with 4 regions of interest

(b) A 4-Threshold Braid Diagram

Figure 2: A simple braid diagram for a network with 4 regions of interest

To study a staging problem, we introduce the concept of a *braid diagram* for (27) (or similarly for (26)) evolving on a network $G = (E, V)$. We illustrate the concept here by constructing a braid diagram for the simple, synthetic example of a network $G = (E, V)$ with $|V| = 4$ nodal ROIs, as shown in Fig. 2a. To begin, let us select some threshold values; suppose we select thresholds $T_1 = 1\%$, $T_2 = 5\%$, $T_3 = 40\%$, and $T_4 = 80\%$. We then seed and run our model (27) (or in general (26)), and we record the time value, t_j, that each ROI obtains a given threshold, T_j, provided it does so. If the threshold value T_j is not achieved, we set $t_j = \infty$. Thus, in our example, with G given by Figure 2a, we have recorded four time values for each ROI in the network G. The abscissa of a braid diagram is labeled with the ROI identifier while the ordinate axis corresponds to the discrete set of threshold values; a line is then drawn, in the vertical direction, connecting the ROI identifier to its position in the ordered list at each threshold. The resulting braid diagram is shown in Figure 2b. In fact, the braid diagram of Figure 2b was generated from solving (27) with an initial seeding of $p_1(0) = 5 \times 10^{-3}$, $p_2(0) = p_3(0) = p_4(0) = 0$, along with the (non-physical) parameters $\rho = e^2$, $\alpha = 1.5 \times 10^{-1}$, and the diffusive weighting scheme (25c) using the (symmetric, non-physical) values of $n_{ij} = n_{ji}$ and $\ell_{ij} = \ell_{ji}$ given in Table 1.

Edge $e_{ij} = (v_i, v_j)$	n_{ij}	ℓ_{ij}
(v_1, v_2)	5×10^{-4}	40
(v_1, v_3)	2×10^{-3}	20
(v_2, v_4)	4×10^{-3}	20
(v_3, v_4)	6×10^{-2}	20

Table 1: Parameters for the braid diagram of Figure 2

Braid diagrams are a powerful visualization of the *ordering of arrival* for a quantity evolving on a network given a suitable set of threshold values; the name of the diagram comes from the visual depictions of permutations of the Artin Braid Group, on n-strands, in topology and knot theory. It is prudent to note that braid diagrams are not necessarily unique in general; for instance, if two ROIs achieve a certain threshold at an equal time (or at $t = \infty$) then the ordering is not uniquely determined. Thus, in practice, it is prudent to: select thresholds that are realized by all ROI; and to use simulation time steps which are small enough to separate ROI values in a computation. In this manuscript, we adhere to both of these requirements and, in this context, a braid diagram allows for a complex arrival-time processes to be visualized in a single image. Indeed, an inspection of Figure2b shows that ROI one achieves each threshold first, followed by ROI three. However, we see that ROI two reaches the 1% and 5% thresholds before ROI four, but that ROI four reaches both the 40% and 80% threshold before ROI two; thus, the *staging patterns* for thresholds $T_1 = 1\%$ and $T_2 = 5\%$ are (v_1, v_3, v_2, v_4) whereas the staging patterns for $T_3 = 50\%$ and $T_4 = 80\%$ are (v_1, v_3, v_4, v_2). Our analysis of braid diagrams will show that staging patterns can depend on model parameter choice, network topology, and the threshold of interest.

For a brain connectome, we will consider multiple resolutions of patient brain connectomes; each of these networks represents 83 distinct cortical, and subcortical, regions of interest in which we will ascertain staging behavior. To construct braid diagrams across resolutions, thereby determining staging patterns, we will use a threshold based on collections of nodes. Let Ω_1, Ω_2, $\ldots$, Ω_N be N distinct regions of interest with $1 \leq N \leq 83$ in the present work. Suppose that a connectome $G = (V, E)$ consists of $|V|$ distinct nodes distributed among the regions Ω_j and that $q_i(t)$, where $i \in \{1, 2, \ldots, |V|\}$ are some normalized biomarker where, for every index i, $q_i(t) \in [0, 1]$. The biomarker associated to the region of interest Ω_j is

$$Q_j(t) = \frac{1}{|\Omega_j|} \sum_{i=1}^{|\Omega_j|} q_i(t), \tag{28}$$

where $|\Omega_j|$ is the number of nodes in region Ω_j. For a given dynamics on the network, we construct braid diagrams based on the time at which the values of the $Q_i(t)$, $i = 1, 2, \ldots, N$, reach a given set of thresholds $T_1, T_2, \ldots, T_M$.

5 Braak staging dynamics for τP seeding

A recent post-mortem study [17] has elucidated the fact that soluble, seed-competent tau-aggregates, i.e. soluble aggregates capable of recruiting and misfolding monomeric tau [17] in a prion-like [18,

Scale	$\max \mathbf{L}_{ij}$ for (25a)	$\max \mathbf{L}_{ij}$ for (25b)	$\max \mathbf{L}_{ij}$ for (25c)	$\max \ell_{ij}$ (mm)
S-33	225.308	9.768	0.564	173.2
S-60	155.128	6.981	0.314	173.2
S-125	155.283	6.990	0.315	174.2
S-250	155.609	7.003	0.315	190.2
S-500	155.290	6.990	0.315	194.6

Table 2: Useful rescaling values for comparisons with other studies

19, 20, 21, 22, 23] fashion, precede the appearance of overt hyperphosphorylated tau NFT pathology along the Braak pathway. We now discuss the results for the Braak staging of toxic τP seeding in the network FKPP model. We investigate the impact of staging due to the three graph Laplacian weighting choices of (25) in addition to assessing the impact of a diffusion dominated, i.e. $\alpha \ll \rho$, and growth dominated, i.e. $\rho \ll \alpha$, assumption. To achieve this last goal, we first assume that α is constant at every connectome node and rescale time $\alpha t \to t$ to obtain

$$\frac{\mathrm{d}p_i}{\mathrm{d}t} = -\beta \sum_{i=1}^{N} L_{ij}\, p_i + p_i(1-p_i), \quad i = 1, \ldots, N, \tag{29}$$

where $\beta = \rho/\alpha$. The two limits correspond to $\beta \ll 1$ (growth dominated) and $\beta \gg 1$ (diffusion dominated). In the first case, we expect the concentration to grow locally before it is diffused and that effect to percolate through the graph. In the second case, we expect diffusion to homogenize rapidly the system and the concentrations at all nodes to increase almost simultaneously. Unlike more advanced, but more complex and computationally expensive, aggregation models [13, 52], (29) does not track a specific aggregate size, only an average concentration of aggregates.

5.1 Graph Laplacian rescalings

Rescalings of the diffusion operator, e.g. in (3), or the graph Laplacian entries $\mathbf{L}_{ij}$, e.g. in (27) or (29) with $\mathbf{L}$ given by (11), have been used by various authors in computational studies. For instance, (3) was used in [53], rescaled by a characteristic length, to fit a growth rate α. In [54] the authors considered (27) with weightings (25a) and (25b); in each case, the rescalings were with respect to $\max \mathbf{L}_{ij}$ to produce a graph Laplacian matrix with entries in $[0, 1]$. A rescaling of the graph Laplacian results in different values for β in (29).

In this manuscript we consider the three weighting schemes (25a)–(25c) for $-10 \leq \ln(\beta) \leq 2$ in order to expose a range of staging dynamics. In each case, the effective units of β vary with each weighting; β in (25a) is a dimensionless number, β in (25b) has units of mm, and β in (25c) has units mm^2. To compare with other studies, values of $\ln(\beta)$, appearing in the figures throughout the remainder of the manuscript, can be rescaled appropriately.

Relevant values for rescalings are listed in Table 2 for each connectome scale. The first three columns report the maximum graph Laplacian entry corresponding to the weighting schemes (25a)–(25c) while the last column reports the maximum length, in millimeters, of the longest fiber length. If a graph Laplacian, $\hat{\mathbf{L}}$, has been rescaled via dividing every entry by a maximal entry then

$$\hat{\beta}\, \hat{\mathbf{L}} = \frac{\hat{\beta}}{\max \mathbf{L}_{ij}} \left(\max \mathbf{L_{ij}}\, \hat{\mathbf{L}} \right) = \beta\, \mathbf{L},$$

and the above identity yields the relation

$$\ln(\hat{\beta}) = \ln(\beta) + \ln(\max \mathbf{L}_{ij}). \tag{30}$$

For instance, consulting Table 2, we see that results reported here for $-10 \leq \ln(\beta) \leq 2$ on the S-33 connectome would correspond to $-4.58 \leq \ln(\hat{\beta}) \leq 7.41$ for the maximal-entry rescaled length-free weightings (25a), $-7.72 \leq \ln(\hat{\beta}) \leq 4.28$ for the maximal-entry rescaled ballistic weightings (25b), and $-10.57 \leq \ln(\hat{\beta}) \leq 1.43$ for the maximal-entry rescaled diffusive weightings (25c). Another way to rescale the graph Laplacian when ballistic (25b) or diffusive (25c) weights are used, is by multiplying every entry by $\max \ell_{ij}$ or $\max \ell_{ij}^2$, respectively. When diffusive weights are used, this approach corresponds to a characteristic length rescaling of the continuous diffusion operator in (3) and then constructing the graph Laplacian, with weighting (25c), using the new characteristic length scale. If a graph Laplacian, $\hat{\mathbf{L}}$, has been already been rescaled in this way, we can retrieve the original form by

$$\hat{\beta}\ \hat{\mathbf{L}} = \left(\hat{\beta} \max \ell_{ij}^r\right) \frac{1}{\max \ell_{ij}^r}\ \hat{\mathbf{L}} = \beta\ \mathbf{L}$$

where $r = 1$ for the ballistic weights and $r = 2$ for diffusive weights. In this case, the corresponding comparison values can be computed via

$$\ln(\hat{\beta}) = \ln(\beta) - r\ln(\max \ell_{ij}). \tag{31}$$

To illustrate we again consider the S-33 connectome and consult Table 2. Then the values $-10 \leq \ln(\beta) \leq 2$ reported in this study would correspond to the values $-15.15 \leq \ln(\hat{\beta}) \leq -3.15$ for a study using a characteristic length rescaling and ballistic coefficients and to $-20.31 \leq \ln(\hat{\beta}) \leq -8.3$ for a study using a characteristic length rescaling and diffusive coefficients. The two methods of scaling in Table 2 do not produce the same dimensionless result for the same weighting scheme on the same connectome. For example, suppose the weighting (25b) is used on the S-500 connectome and that $\ln(\beta) = -2$. The maximum-entry rescaling relation (30) produces

$$\ln(\hat{\beta}) = -2 + \ln(6.99) = 5.555 \times 10^{-2},$$

whereas the maximum length rescaling, with $r = 1$ due to the weight selection (25b), gives

$$\ln(\hat{\beta}) = -2 - \ln(194.6) = -7.27.$$

To maintain consistency throughout this manuscript, we will use a static range of values for $\ln(\beta)$, for all connectomes, and avoid choosing a particular rescaling; instead, we refer to Table 2 where needed. We note that the graph Laplacian for one scale, e.g. S-33, is a fundamentally different discrete operator, with different dimensions and topological connectivity patterns, than that of another scale, e.g. S-500. As such, we avoid directly comparing values of β across scales; only qualitative observations will be made.

5.2 Connectome regions, and initial seeding, for a Braak staging analysis

We follow previous authors [17, 41] in classifying the primary Braak stages by the regional deposition patterns of soluble seed-competent τP; these stages are enumerated in Table 3.

Braak Stage I	entorhinal cortex
Braak Stage II	hippocampus
Braak Stage III	posterior parahippocampal gyrus
Braak Stage IV	anterior cingulate
Braak Stage V	visual association cortex
Braak Stage VI	primary visual cortex

Table 3: Braak Staging Regions, as reported in [17, 41].

The regions in Table 3 are a close match to the labels used, in the parcellation process, to generate [37, 39] the connectomes discussed in Section 2.2; however, the match is not exact. We therefore use, in this manuscript, a five-stage Braak connectome staging process. The connectome Braak stages are listed in Table 4; the primary differences are that Braak stage IV now combines the rostral and caudal anterior cingulate, and Braak stages V and VI are amalgamated into a final stage and approximated by the presence of deposition in the cuneus, pericalcarine cortex, lateral occipital cortex, and lingual gyrus. We note that all of the connectomes are connected undirected networks and we leave the choice of weights open as to compare different modelling assumption.

Staging Region	Parcellation Label	Regional nodes by resolution				
		S-33	S-60	S-125	S-250	S-500
Number of nodes		83	129	234	463	1015
Braak Stage I	entorhinal (cortex)	2	2	2	2	5
Braak Stage II	hippocampus	2	2	2	2	2
Braak Stage III	parahippocampal (gyrus)	2	2	2	6	12
Braak Stage IV	rostral anterior cingulate, caudal anterior cingulate	4	4	4	9	20
Braak Stage V	cuneus, pericalcarine (cortex), lateral occipital (cortex), lingual (gyrus)	8	13	23	50	100

Table 4: Connectome Braak Staging, subject to parcellation labels of [37, 39]. S-33 stands for Scale-33 network and so on.

The *desired staging* behavior is therefore Braak I (purple)→Braak II (green)→Braak III (gold)→Braak IV (blue)→Braak V (red). We will use the regional biomarker, for each Braak staging region Ω_j, defined by (28); that is,

$$Q_j(t) = \frac{1}{|\Omega_j|} \sum_{i=1}^{|\Omega_j|} p_i(t), \tag{32}$$

where the regions and the number of nodes are defined in Table 4.

The connectomes span the five scales of resolution detailed in Section 2.2. The number of nodes in each of the five Braak staging regions are given in Table 4. The connectome Braak stage regions for the lowest (Scale-33) and highest (Scale-500) resolution computational connectomes are shown in Figure 3. In Figure 3, the colored regions correspond to the Braak stages; from left to right, these are purple (Braak I), green (Braak II), gold (Braak III), blue (Braak IV), and red (Braak V).

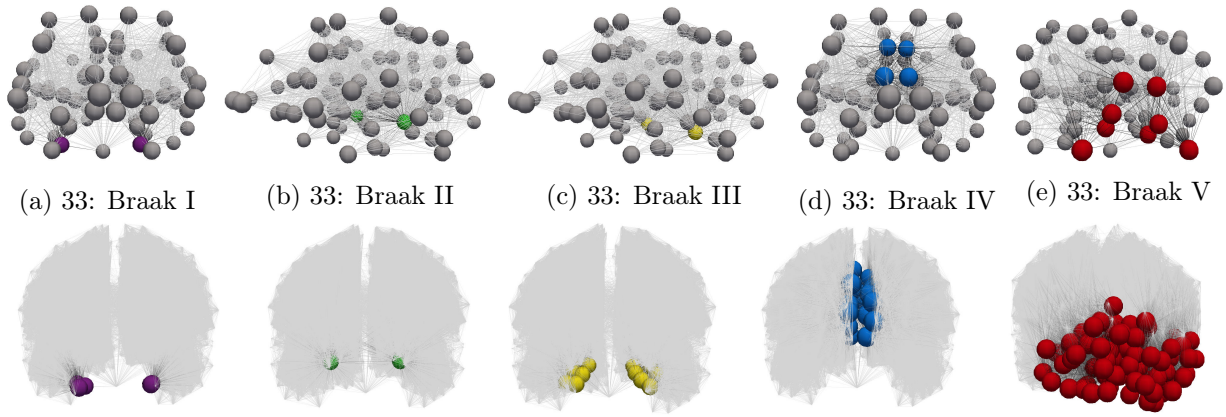

(a) 33: Braak I (b) 33: Braak II (c) 33: Braak III (d) 33: Braak IV (e) 33: Braak V

(f) 500: Braak I (g) 500: Braak II (h) 500: Braak III (i) 500: Braak IV (j) 500: Braak V

Figure 3: Connectome Braak Staging Regions. Scale-33 (top) and Scale-500 (bottom) connectomes.

We remark that extraneous nodes for the scale-500 case, Figure 3 bottom row, have been visually suppressed to increase the visibility of the Braak regions. As each Braak region consists of multiple nodes, staging thresholds are measured according to (28) for each region. All of the computations in the remainder of the manuscript (i.e. those in Section 5.3, Section 5.4, and Section 6) use the same initial (seeding) conditions. Namely, the entorhinal cortex region is seeded with a total of 0.5% toxic protein

$$\sum_{i \in \Omega_{\mathrm{EC}}} p_i(0) = 5 \times 10^{-3},$$

distributed uniformly amongst the nodes $v_i \in \Omega_{\mathrm{EC}}$. The initial value for all other nodes in the connectome graph is set to zero.

5.3 Staging of τP seeds depends on resolution, weighting, and parameter choice

It has been observed that that soluble, seed-competent tau aggregates precede tau NFT pathology [17]. Therefore, we use biomarker thresholds for the Braak staging measures given (28). We highlight several heuristic observations regarding the effect of connectome , weighting, and parameter choices. In particular, we show now that each of these choices alter the staging pattern depending on the choice of threshold.

Connectome resolution alters observed Braak staging Figure 4 shows the results of solving (29) with $\ln(\beta) = 3$, on the Scale-33 connectome, and using diffusive weights. The abnormality plots and braided staging diagrams tell an interesting story. First, we notice that, in the diffusion dominated regime, the abnormality curves show a sharp, nearly-simultaneous, increase for the case of the Scale-33 connectome (Figure 4a) whereas the abnormality curves spread farther apart and show clear separation at the resolution of the Scale-500 connectome Figure 4c. The Braid diagrams for seed competent τP staging show a change in the Scale-33 connectome (Figure 4b) as the staging detection threshold crosses from 20% to 30%. Conversely, the staging pattern for the Scale-500 resolution simulation is uniform (Figure 4d). However, it is worth noting that neither the Scale-33

or the Scale-500 resolution staging patterns are the desired Braak staging. In fact, in Section 5.4, we will see that this observation always holds true in the diffusion dominated regime.

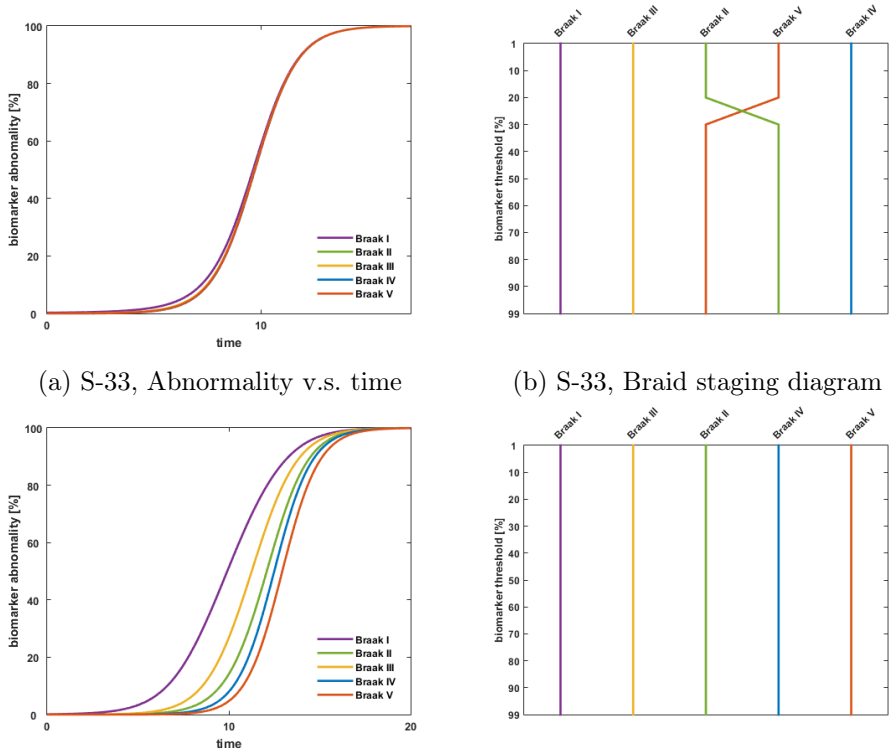

(a) S-33, Abnormality v.s. time

(b) S-33, Braid staging diagram

(c) S-500, Abnormality v.s. time

(d) S-500, Braid staging diagram

Figure 4: Diffusion-dominated Braak staging, Scale-33 (top) v.s. Scale-500 (bottom)

Weighting choice alters Braak staging Figure 5 shows the effect of weight selection on computational Braak staging for the case of growth-dominated dynamics, with $\ln(\beta) = -3$ using the highest resolution (Scale-500) connectome. The length-free weighting scheme (25a), analogous to weighting by connection strength, is uniform for all threshold values; however, it does not produce the desired Braak staging. The ballistic weights (25b) produce the correct staging pattern for a biomarker threshold of 1% but quickly switches to an incorrect staging pattern for thresholds of 10% or greater (Figure 5b). Finally, we note that the diffusive weights give a uniform braid diagram for all biomarker thresholds, and is consistent with the histopathologically expected progress (Figure (5c)).

Parameter regimes alter Braak staging Finally, we show that altering balance of the growth-versus-diffusion dominated regime, i.e. β, changes the computationally-observed Braak staging. Length-free weights have proven to be a popular focus in the literature for diffusion-only models (c.f. [7, 9, 8, 10, 50]) and, typically, a low-resolution connectome is used to reduce computational costs. Thus, we use this opportunity to showcase the τP seed staging implications for length-free graph Laplacian weightings in the case of diffusion-dominated and growth-dominated regimes;

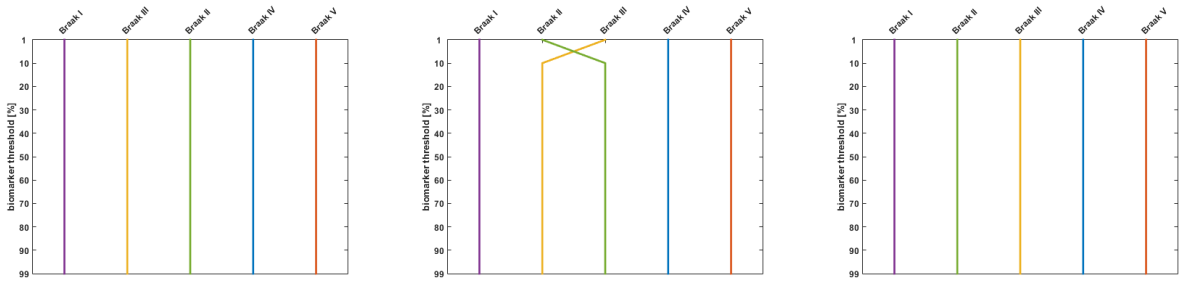

(a) Length-free weights (25a) (b) Ballistic weights (25b) (c) Diffusive weights (25c)

Figure 5: Weight selection perturbs computational Braak staging.
Dominant growth, Scale-500. Length-free (left), Ballistic (middle) and Diffusive (right) weightings.

for both the lowest and highest resolution connectomes. An immediate observation is that the low-resolution computational Braak staging in a diffusion-dominated regime, with $\ln(\beta) = 2$, is incorrect for every biomarker threshold, but also exhibits extreme variations with respect to the biomarker threshold level (Figure 6a). As the parameter regime trends towards one dominated by growth, c.f. Figures 6b and 6c, the observed Braak staging on the Scale-33 connectome does not vary as much. The growth-dominated regime (Figure 6b) is relatively uniform but exhibits uniformly incorrect τP seed staging for all thresholds; however, in the case of the extreme growth-dominated regime (Figure 6c), where $\ln(\beta) = -8$, we do indeed observe the desired Braak staging of τP seeding for biomarker thresholds less than 30%.

The Scale-500 connectome simulations in Figure 6 show both the impact of the model regime parameter in addition to the importance of the increased resolution in the case of length-free weights. First, we notice that the diffusion-dominated regime is still beset with somewhat erratic behavior in the case of length-free weights (Figure 6d). Second, we observe increased stability in the observed staging pattern, as $\ln(\beta)$ decreases, with an increase in connectome resolution; both the growth dominated and extreme-growth dominated cases (Figures (6e) and (6f)) are immutably uniform for every threshold value. Computational Braak staging in the growth dominated (Figure (6e)) regime with $\ln(\beta) = -3$ is, however, uniformly incorrect; conversely, in the extreme growth regime (Figure (6f)) the staging is uniformly correct with respect to the threshold value.

5.4 Braid surfaces for staging patterns

The observations of Section 5.3 indicate that connectome Braak staging, even for a simple model, is a complex problem influenced by several modeling choices. In this section we introduce braid surfaces as a method of visualizing a parametrized family of braid diagrams; thus simplifying the analysis of a large set of staging results. The various connectome Braak staging patterns encountered are identified in Table 5 alongside their identifying color in the braid surface diagrams. The horizontal axis of a braid surface denotes the biomarker abnormality threshold while the vertical axis indicates the value of $\ln(\beta)$; higher values indicate increasingly diffusion-dominated evolution while lower values indicate domination by the growth process. Recall that, as discussed in Section 5.2, the initial seeding used for all computations is a 0.5% toxic seed distributed uniformly across all nodes of the entorhinal cortex (Braak staging region I) with zero elsewhere.

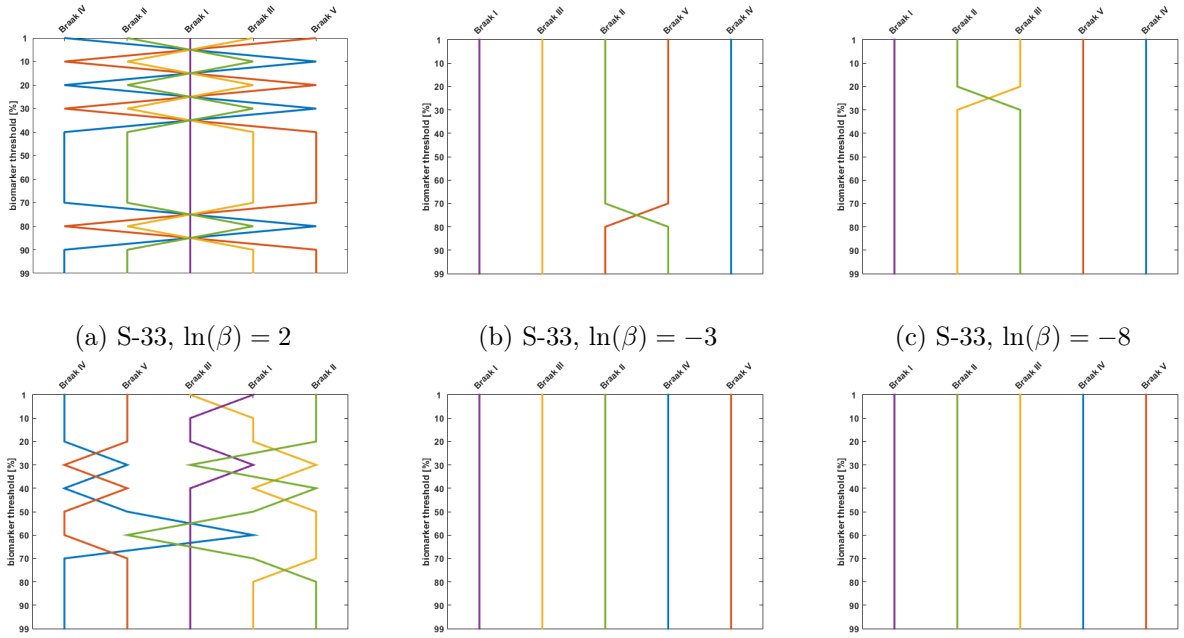

(a) S-33, $\ln(\beta) = 2$ (b) S-33, $\ln(\beta) = -3$ (c) S-33, $\ln(\beta) = -8$

(d) S-500, $\ln(\beta) = 2$ (e) S-500, $\ln(\beta) = -3$ (f) S-500, $\ln(\beta) = -8$

Figure 6: Regime selection perturbs computational Braak staging. Length-free weighting (25a) on the Scale-33 (top row) and Scale-500 (bottom row) connectomes. Diffusion (left column), growth (middle column), and extreme growth (right column) dominant regimes.

From Table 5 we see that the desired Braak staging is denoted by a ○ coloring. Moreover, we have characterized the various staging patterns as 'consistent', 'pathological', 'uniform' and 'erratic'. A pattern is *consistent* if the first staged region coincides with Braak region I where the initial seeding for the model takes place; the staging pattern is referred to as *pathological* if this is not the case; the term 'uniform' means that the pattern generally appears for a suitable range of contiguous biomarker thresholds and parameter values; the term 'erratic' implies that the pattern is observed erratically as as parameter values are slightly altered. We have also assigned a distance to the various stages by considering the number of transpositions necessary to bring a particular staging pattern to the desired staging sequence.

Length-free weights show poor τP seed staging for all connectome resolutions Previous studies have used length-free weights, e.g. based on connection strength or similar measure, to ascertain various correlations with pathology such as proteopathy propagation and atrophy [7, 9, 8, 10, 50]. Furthermore, these early studies have used low-resolution connectomes with few nodes (corresponding to anatomical regions of interest). The results of Figure 7 call into question the use of such models for accurately ascertaining a histopathologically consistent Braak staging. First, note that the correct histopathological ○ Braak connectome staging on the low resolution connectome only occurs in the extreme growth-dominated regime and only for a biomarker threshold of ≈95% (c.f. Figure (7a)). The prominence of the correct Braak staging region grows with increased resolution. However, we note that these regions are all in the parameter regime of significant growth

Legend color	Braak staging pattern	Distance
Consistent and uniform staging patterns		
	I → II → III → IV → V	0
	I → II → III → V → IV	1
	I → III → II → IV → V	1
	I → III → II → V → IV	2
	I → III → V → II → IV	3
Consistent and erratic staging patterns		
	I → III → V → IV → II	4
	I → III → IV → V → II	3
	I → III → IV → II → V	2
	I → IV → II → III → V	2
	I → IV → III → II → V	3
	I → IV → V → III → II	4
	I → IV → III → V → II	4
	I → V → III → II → IV	4
Pathological and erratic staging patterns		
	Beginning at Braak Stage II	≥ 1
	Beginning at Braak Stage III	≥ 2
	Beginning at Braak Stage IV	≥ 3
	Beginning at Braak Stage V	≥ 4

Table 5: Braid surface Braak staging paradigms. The distance corresponds to the transposition distance to the desired Braak pattern.

($-10 \leq \ln(\beta) \leq -6$), and depend on the selected threshold. More succinctly, even as the connectome scale increases, the significant growth regime is never free from a staging pattern which is distance one away from the desired result (either ● or ●) depending on the connectome resolution and the selecting τP seeding threshold selected for the staging dynamics. As a final observation, we note that, across all connectome resolutions, an increase in the dominance of diffusion over growth leads to an increase in both erratic and pathological staging patterns. This larger scale braid-surface observation, for length-free weightings, is consistent with the individual braid diagram dynamics observed in Figures (6a)–(6c). This observation implicitly calls into question the use of diffusion-only models [7, 9, 8, 10, 50] to evolve τP proteopathy where 'connection strength' type weightings, analogous to (25a), are used; at least in so far as a Braak staging is concerned.

A ballistic weighting qualitatively improves τP seed staging results For the case of ballistic weights, we observe an improvement in the observed desirable Braak staging results; in particular, the surface area of the histopathologically accurate ● Braak connectome staging pattern is increased at every scale. For instance, a comparison of the lowest resolution S-33 length-free results (Figure 7a) to the S-33 ballistic results (Figure (8a)) shows a dramatic improvement; the latter achieves the correct staging across a wider β-parameter regime and for more values of the biomarker threshold. We note, though, that the ballistic weighting scheme does share two attributes in common with the length-free weighting: first, if diffusion is on par with, or dominant over,

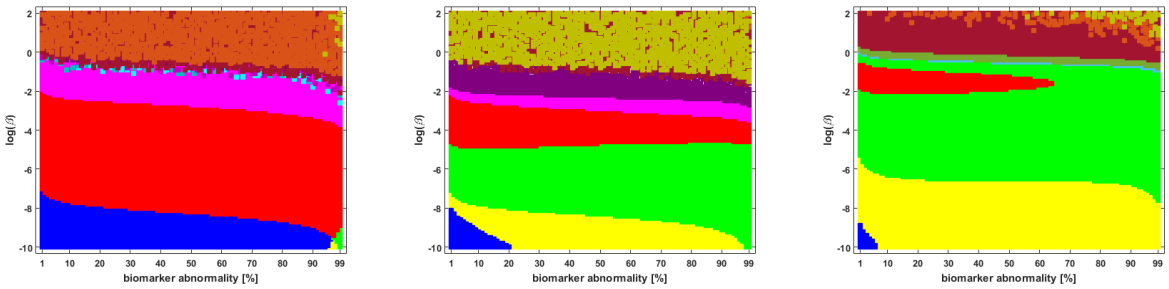

(a) S-33 (b) S-125 (c) S-500

Figure 7: Braid surface for length-free weights for connectome of increasing resolution. Biomarker abnormality (x-axis) v.s. $\ln(\beta)$ y-axis.

growth one does not observe the correct τP seeding pattern for any biomarker threshold; second, ballistic weightings are beset with the appearance of both erratic and pathological staging patterns as diffusion plays a more prominent relative role.

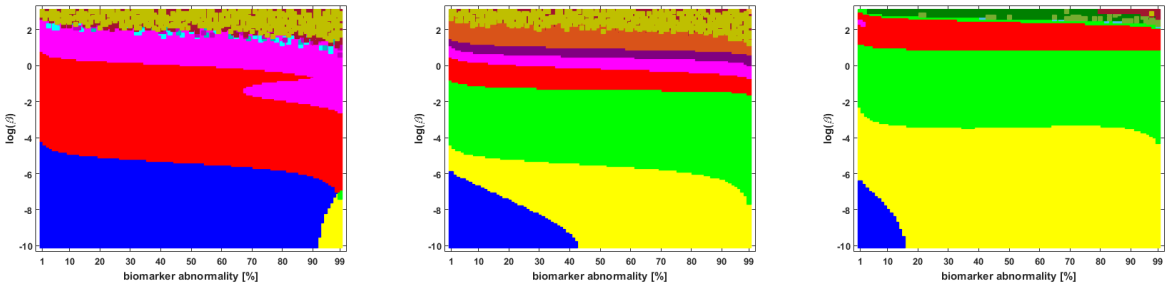

(a) S-33 (b) S-125 (c) S-500

Figure 8: Braid surface for ballistic weights for connectome of increasing resolution. Biomarker abnormality (x-axis) v.s. $\ln(\beta)$ y-axis.

A diffusive weighting further improves observed τP seed staging results Figure 9 shows the results for connectome staging, across resolutions, for the use of diffusive graph Laplacian weights (25c) in the τP seeding model of (29). In particular, we see that the desired ● Braak staging has the largest prominence across all connectome scales (S-33 to S-500) when compared to both length-free (Figure 7) and ballistic (Figure 8) weighting paradigms. Furthermore, it is evident that increasing the connectome resolution provides the correct histopathological connectome staging for the broadest range of biomarker threshold values; indeed, the S-500 resolution connectome (Figure (9c)) yields the correct staging pattern for all biomarker levels when the balance of diffusion-vs-growth satisfies $0 < \ln(\beta) < 4$. We can also note, again, the trend that diffusion-prominent ($\ln(\beta) > 0$) instances of the model generally fail to yield the correct τP seed Braak staging at all connectome resolutions and for all biomarker thresholds. In particular, the lowest resolution connectomes (c.f. Figure 9a for S-33 and similarly for S-60) are constituted by significant regions indicating a considerably perturbed (● and ●) staging pattern from that of the physiologically

desirable ○ Braak staging paradigm. However, we do note that the use of diffusive weights yields staging results which are uniform across all connectome scales. More specifically, in contrast to both Figure 7 and Figure 8, Figure 9 does not display oscillations in the observed Braak staging with small perturbations, in either β or biomarker threshold, at any resolution; Figure 9 is also devoid of any pathological Braak staging patterns (c.f. Table 9) irrespective of both β and the selected biomarker threshold.

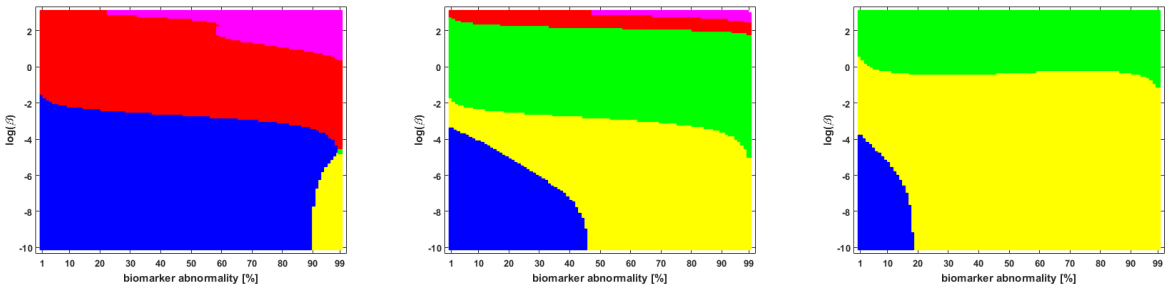

(a) S-33 (b) S-125 (c) S-500

Figure 9: Braid surface for diffusive weights for connectome of increasing resolution. Biomarker abnormality (x-axis) v.s. $\ln(\beta)$ y-axis.

6 Braak staging dynamics for τP neurofibrillary tangles

Next, we extend the τP seeding model (3) by coupling it with a pathology accumulation equation [7, 8]. First, following [44], we define a simple *damage* marker of NFT pathology accumulation by

$$q(t) = \int_0^t \hat{\delta} p(1 - q(s))\, \mathrm{d}s,$$

where $\hat{\delta}$ is an NFT pathology accumulation rate which we assume is proportional to the growth rate; i.e. $\hat{\delta} = \delta\alpha$. Discretizing on the connectome, and rescaling in time as in Section 5, leads to the following coupled network NFT pathology model

$$\frac{\mathrm{d}p_i}{\mathrm{d}t} = -\beta \sum_{i=1}^{N} \mathbf{L}_{ij}\, p_i + p_i(1 - p_i), \tag{33a}$$

$$\frac{\mathrm{d}q_i}{\mathrm{d}t} = \delta p_i \left(1 - q_i\right), \tag{33b}$$

where δ is constant and $p_i(s)$ denotes the τP seed evolution in the connectome (parcellated region) node v_i. We will once more analyze the connectome Braak staging, according to Tables 3 and 4, and evaluate the impact of connectome resolution, biomarker threshold based on the nodal damage values

$$Q_j(t) = \frac{1}{|\Omega_j|} \sum_{i=1}^{|\Omega_j|} q_i(t), \tag{34}$$

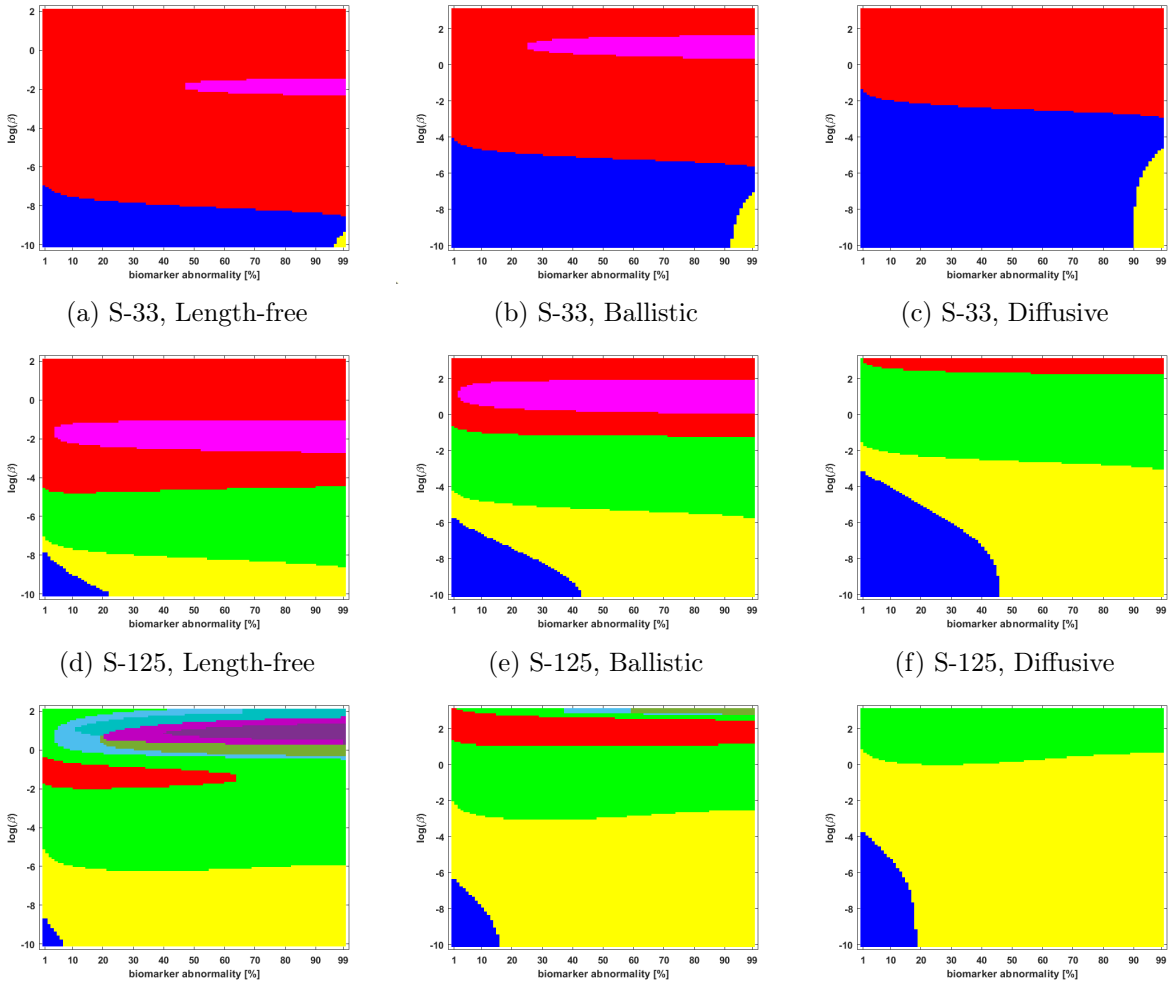

(a) S-33, Length-free (b) S-33, Ballistic (c) S-33, Diffusive

(d) S-125, Length-free (e) S-125, Ballistic (f) S-125, Diffusive

(g) S-500, Length-free (h) S-500, Ballistic (i) S-500, Diffusive

Figure 10: Braid surfaces for τP NFT connectome Braak staging, $\delta = 1$. Biomarker abnormality (x-axis) v.s. $\ln(\beta)$ y-axis.

where the regions and the number of nodes are defined in Table 4. As discussed in Section 5.2, we use an initial seeding of a total of 0.5% toxic protein, i.e. $p(t)$ of (33a), distributed uniformly amongst the vertices of the entorhinal cortex. The initial conditions for the NFT marker variable, $q(t)$ of (33b), are set uniformly to zero in every vertex of the connectome.

6.1 Staging of τP NFT depends on resolution, weighting, and parameter choice

We consider the Braak staging of NFT for $\delta = 1$ in (33b). As in Section 5, we focus here primarily on the impact of connectome resolution, graph Laplacian weightings, and the balance of diffusion-versus-growth as reflected by the value of $\ln(\beta)$ in (33a); the impact of varying δ will be covered in the next Section.

Connectome resolution alters NFT staging Figure 10 clearly demonstrates that connectome resolution can alter computationally observed staging patterns. Overall, as connectome resolution increases, the presence of incorrect staging patterns diminishes and the prominence of undesirable staging patterns is reduced. That is, the surface area of desired staging (●), or nearby transpositional paradigms (● or ●), staging patterns increases as connectome resolution increases. Overall, when growth is the dominant factor in the model, i.e. when $\ln(\beta) \leq -2$, lower resolution connectomes (e.g. S-33, S-60 (not shown) or S-125) produce the least desirable staging results, in terms of surface area, for every choice of weighting.

Weighting choice alters NFT staging In Figure 10, we see that desired staging (●) surface area qualitatively improves by choosing ballistic weights over length-free weights and improves again with the choice of diffusive weights over ballistic weights. In addition, there is an overall decrease in more distant (●, ●, ●, etc), staging pattern surface area as one moves from length-free to diffusive weights. It is important to note that this overall trend is not necessarily true for a fixed incorrect staging pattern in every β subdomain and at every resolution. For instance, consider the three weighting schemes on the S-33 connectome (Figure 10, top row) and the diffusion prominent regime $0 < \ln(\beta)$. In this case, moving from length-free weights to ballistic weights actually increases the surface area of the incorrect ● Braak staging within this region. Of course, the region of increasing diffusive dominance for all connectome resolutions are also essentially uniformly incorrect, for all weighting paradigms considered.

Observed NFT staging differs with parameter regime We also observe qualitative differences between the regimes of dominant growth ($\ln(\beta)$ near 1 or 2), balanced diffusion and growth ($\ln(\beta)$ near 0), and dominant growth ($\ln(\beta)$ near -2 or -3). In general, we note that the regime of dominant growth is defined uniformly by incorrect staging patterns for the base case of $\delta = 1$. The growth dominated regime, overall, shows the most favorable results. We note that, overall, most all of the correct ● Braak staging pattern surface area occurs for $\ln(\beta) < 0$ and that the correct ● Braak staging regions tend to shift upwards with an increase in connectome resolution (columns of Figure 10) and an increase in the contribution of length to the Laplacian weights (rows of Figure 10); the largest region where the correct ● Braak staging pattern holds for all biomarker levels occurs in Figure 10i for $-4 < \ln(\beta) < 0$.

The most favorable overall NFT staging results Our results so far suggest that the highest resolution connectome with the diffusive weights Laplacian show the most favorable result in the sense that this regime it is consistent with Braak staging for large ranges of β (Figure 10i). In general, the use of diffusive weights appears to provide the largest surface area of the correct staging pattern (●) at every connectome resolution.

6.2 Braak staging of NFT is perturbed by pathology growth rate

Next, we study the effect of NFT accumulation by fixing the parameter β and varying δ.

NFT τP staging in the regime of dominant diffusion We choose $\ln(\beta) = 2$ to represent this regime. Braak staging, for varying δ and abnormality thresholds, are shown in Figure 11. The correct ● Braak staging pattern is absent from nearly every connectome resolution, and weighting scheme, and for every value of δ; the lone exception is the S-500 connectome with diffusive weights and a choice of δ in the range of $2 \leq \ln(\delta) \leq 3$ and a high biomarker threshold. Otherwise, a general trend of improved staging is observed with increased connectome resolution and from length-free to ballistic weights and again to diffusive weights. This suggests that if τP diffusion is dominant, and NFT do not aggregate quickly, then achieving a measure of the desired (●) staging is impeded.

NFT τP staging in the regime of dominant growth The dependence of connectome Braak staging on δ in a regime of dominant growth, $\ln(\beta) = -3$, is shown in Figure 12. In general, we see the continuation of the trend, seen also for τP seeding, that connectome τP NFT Braak staging improves as growth takes prominence over diffusion. We first note that the choice of length-free weights (Figure 12, left column) do indeed improve their Braak staging by moving closer, with respect to transpositional distance, to the correct staging ● pattern with increasing connectome resolution. However, the length-free weights produce uniformly incorrect connectome Braak staging results and varying δ has little impact, on this observation, overall. We note that varying δ also has no impact on S-500 results for diffusive weights, but that these results are already uniformly correct. It can also be observed, as in every previous case, that the diffusive weighting scheme once again produces the largest surface area for the correct Braak connectome staging ● pattern.

It is once more discerned that increasing the connectome resolution has a positive impact on improving the observed staging patterns; the growth dominant regime is no different and results improve as one moves from top to bottom within any column of Figure 12. It is interesting to note that, unlike the diffusion-dominant (c.f. Figure 11) or balanced regime cases, increasing the NFT aggregation rate (δ) may not always produce an improved Braak staging across all biomarker thresholds. In Figure (12f) we see that both increasing, and decreasing, from $\ln(\delta) = 0$ can lead to an incorrect Braak staging (● or ● respectively) depending on the biomarker detection threshold. Conversely, we do see (Figure 12h) that an increased δ has a regularizing effect on the staging for ballistic weights for the highest resolution connectome; a decreased NFT aggregation rate, here, yields an undesirable staging.

7 Concluding remarks

The results presented in this paper are threefold. First, at the theoretical level, when modeling diffusion on a network of a physical substance, the requirements of mass conservation and no-flux in

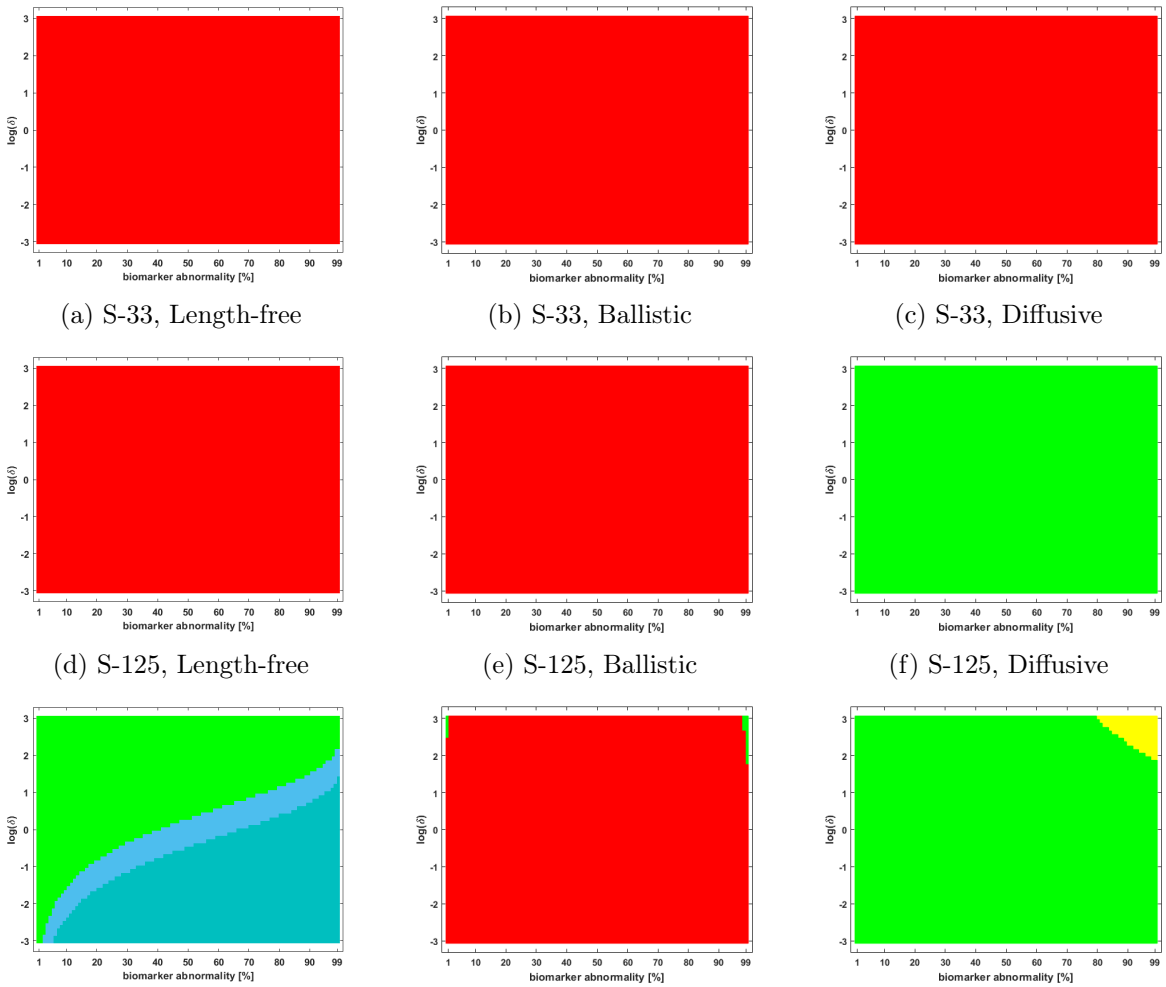

(a) S-33, Length-free (b) S-33, Ballistic (c) S-33, Diffusive

(d) S-125, Length-free (e) S-125, Ballistic (f) S-125, Diffusive

(g) S-500, Length-free (h) S-500, Ballistic (i) S-500, Diffusive

Figure 11: δ Braak staging τP NFT pathology with dominant model diffusion ($\ln(\beta) = 2$). Biomarker abnormality (x-axis) v.s. $\ln(\delta)$ y-axis.

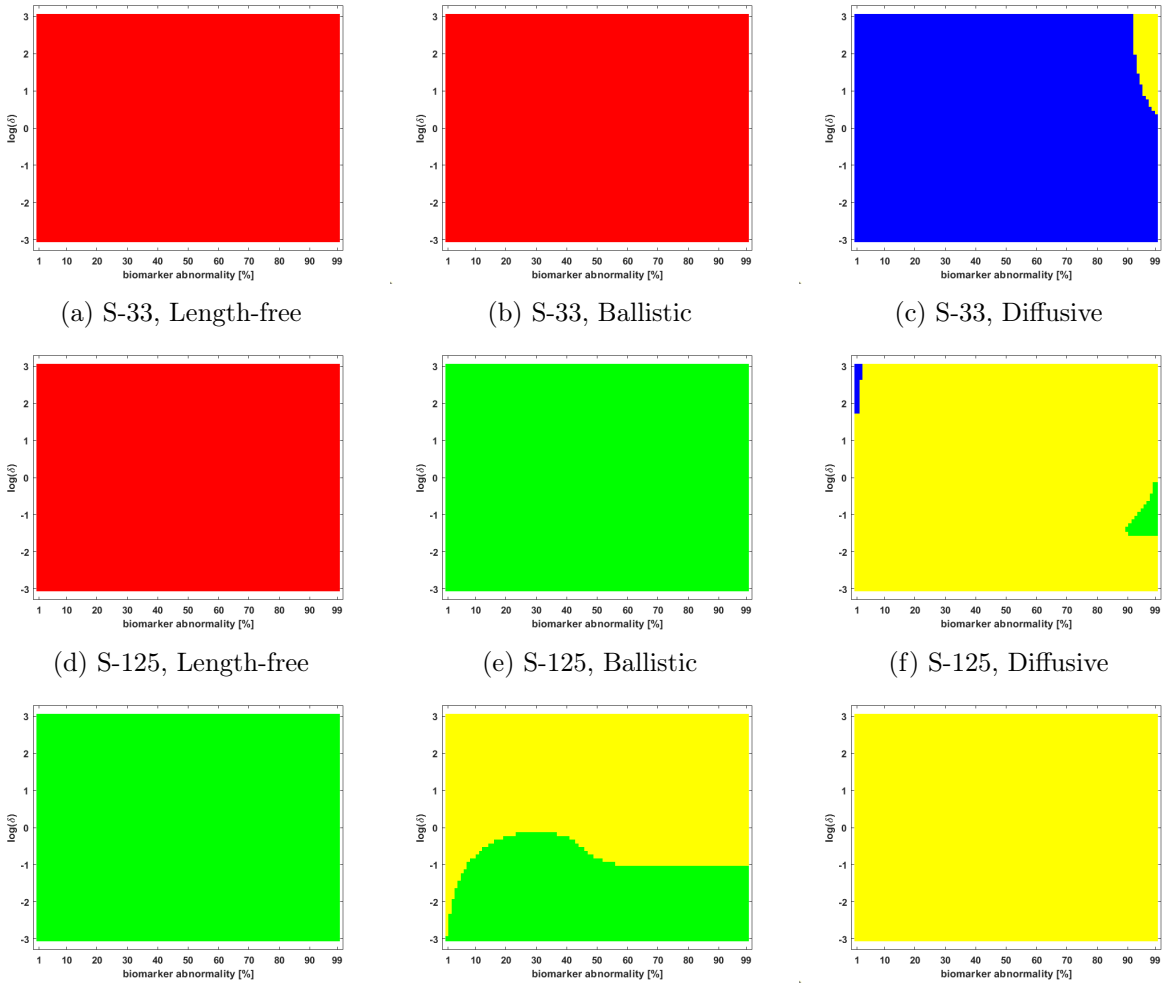

(a) S-33, Length-free (b) S-33, Ballistic (c) S-33, Diffusive

(d) S-125, Length-free (e) S-125, Ballistic (f) S-125, Diffusive

(g) S-500, Length-free (h) S-500, Ballistic (i) S-500, Diffusive

Figure 12: δ Braak staging τP NFT pathology with dominant model growth ($\ln(\beta) = -3$). Biomarker abnormality (x-axis) v.s. $\ln(\delta)$ y-axis.

the absence of a concentration gradient imply that the only possible choice for the diffusion operator is the standard graph Laplacian (possibly suitably modified to account for variation of volume in different regions). It may be tempting, for computation reasons, to use a normalized Laplacian. However, this will lead, invariably to the violation of fundamental physical requirements and should be avoided. This result, of course, does not apply to other spreading processes on graphs that are not related to a physical substance (e.g. information transfer). Yet, the same question should be asked for these other processes and the task of identifying the physically correct graph Laplacian has been mostly ignored.

Second, our study provides potential insights into a class of AD regimes where particular τP staging results would be possible; our results suggest, in particular, that a growth regime is important for observing Braak staging. This observation has been corroborated by other authors in related studies. In [53], the authors fitted experimental data, across Braak stages III-VI, to (3) under a radial symmetry assumption. Their investigation suggests that, in Alzheimer's disease, it is primarily growth that drives staging at Braak III and beyond. A few years of tau positron emission tomography (PET) data, for several patients, has been used [54] to fit estimated growth and diffusion parameters of (27) using the lowest resolution (S-33) connectome alongside a graph Laplacian based on a ballistic (c.f. (25b)) weighting scheme and maximum-entry rescaling. The study reported a mean value of $\alpha = 0.21$ (per year) and a mean value of $\rho = 0.34$ (with units of yr^{-1} due to the graph Laplacian rescaling). Their reported value of $\hat{\beta}$ is then $\hat{\beta} = \rho/\alpha = 1.62$. Table 2 shows that the maximal entry for the S-33 connectome, with weighting (25b), is 9.768. The corresponding value of $\ln(\beta)$, used in this study, follows from (30) as

$$\ln(\beta) = \ln(\hat{\beta}) - \ln(9.768) = -1.8.$$

The above data-inferred [54] value for $\ln(\beta)$ falls within the growth dominated regime as defined in the present study; a regime that favors growth over diffusion appears, initially, to be supported by PET data.

Third, and most importantly, we have demonstrated that a number of factors can impact an observed staging process over a connectome and we have introduced new tools to visually assess staging as a function of problem features. In particular, the connectome resolution, graph Laplacian weighting scheme, model parameter regime and the selected biomarker threshold can all alter the realization of a particular simulated staging pattern. We have considered a simple Fisher-KPP model (27) in our approach here. However, the observations above are general; our work suggests that authors using network models for specific diseases should carefully check that their model setup (e.g. connectome resolution, weighting scheme, etc) provides for any characteristic staging patterns corresponding to that disease. To assist in this general task, we have introduced the concept of braid diagrams and braid surfaces. Braid diagrams provide a detailed look at a staging pattern as a function of a single problem parameter; braid surfaces provide a broad look at how changes in a multi-parameter family can perturb an observed staging pattern.

We realize that, in the process of establishing modeling guidelines for the spread of neurodegenerative diseases, our results are in opposition to most existing models. That is, most contemporary models typically use at least one of: a normalized graph Laplacian; a low-resolution connectome; non-diffusive graph Laplacian weights; or parameters that favor the diffusion dominated regime (most of them have no growth at all). Our study does not contradict any of these previous studies as, to the best of our knowledge, it is is the first to address these issues. Our investigation commenced with the observation that different authors make different modeling choices. Many of these

choices, while often quite appealing for their intuition, are not justified nor were their implications investigated. It should be clear that our goal is not to criticize these models. They have played an immensely important role in establishing new ideas in the field; they have also, at times, shown excellent correlation with imaging data. Yet, as the field gains maturity, it is imperative that we revisit various assumptions and subject them to a suitable scrutiny. Our study shows that these choices matter both on a theoretical and a practical basis.

It is important to close with with a brief reflection on Braak staging. Most importantly, Braak staging is not a universal truth. There are refined spreading staging patterns, with many intermediate stages, that occur in different subtypes of dementia. For this reason, we have chosen here the most basic staging patterns that occur in typical cases of AD. Moreover, the question of measuring a Braak staging is subordinate to a choice of biomarker percentage. For instance, low concentrations of τP seeds have been observed [17, Figure 2, Figure 3] in later-stage, Braak III–Braak V, regions for patients classified as Braak I. This means that requiring a computational model to respect τP seeding at a low ($T = 1\%$) threshold is likely to be overly restrictive. Data suggests that some τP Braak staging variation exists between patients [17]. In addition, determining a precise Braak staging from tau PET data can pose a challenge due to a number of error sources [54]. These include errors from automatic segmentation, off-site binding, and limited (PET) image resolution, among others.

Nevertheless, we have illustrated that strictly enforcing a Braak staging, for any selected biomarker percentage, can be done if one carefully balances the various model traits. We do not necessarily advocate that this should be done for low biomarker thresholds, or for both τP and NFT simultaneously; this is a question of appropriate model selection subservient to a particular study. For example, in light of experimental evidence, one may choose to relax a Braak staging requirements for τP seeds while strictly enforcing it for NFT. Our study shows that one can achieve such a model by selecting the highest resolution (S-500) connectome, diffusive weights (25c), and any τP seed biomarker threshold; this choice produces a ● seed staging (c.f. Figure 9c). To enforce Braak staging for NFT, we would then select $\ln(\delta) = 3$ and an NFT biomarker percentage of 90%; these additional choices produce the correct ● NFT staging (c.f. Figure 11). Allowing the parameters $\ln(\beta)$ and $\ln(\delta)$ to vary in some range around the above values could be used to reproduce seed patterns similar to [17] while still maintaining an overall Braak NFT staging.

The methods presented here are general and can be easily adapted for other seeding locations, other conditions, non-homogeneous systems and so on. Yet, the basic principles that a model should, to some extent, be physically admissible and consistent with a basic observation of staging for a given condition remain. These constraints should be enforced before specific values of the parameters for a model are chosen. Our novel braid diagram techniques are ideal for this task and should be adopted, hopefully, as a generic computational tool for the theoretical study of neurodegenerative diseases.

Acknowledgement

The work of A. Goriely was supported by the Engineering and Physical Sciences Research Council grant EP/R020205/1. The work of P. Putra was partially supported by the Engineering and Physical Sciences Research Council grant EP/R020205/1 to AG. The work of T. Thompson was supported partially the John Fell Oxford University Press Research Fund grant 000872 (project

code BKD00160) to TT, and partially by the Engineering and Physical Sciences Research Council grant EP/R020205/1 to AG.

References

[1] Y. Iturria-Medina, R. C. Sotero, P. J. Toussaint, A. C. Evans, and A. D. N. Initiative, "Epidemic spreading model to characterize misfolded proteins propagation in aging and associated neurodegenerative disorders," *PLoS computational biology*, vol. 10, no. 11, p. e1003956, 2014.

[2] M. X. Henderson, E. J. Cornblath, A. Darwich, B. Zhang, H. Brown, R. J. Gathagan, R. M. Sandler, D. S. Bassett, J. Q. Trojanowski, and V. M. Lee, "Spread of α-synuclein pathology through the brain connectome is modulated by selective vulnerability and predicted by network analysis," *Nature neuroscience*, vol. 22, no. 8, p. 1248, 2019.

[3] Y.-Q. Zheng, Y. Zhang, Y. H. Yau, Y. Zeighami, K. Larcher, B. Misic, and A. Dagher, "Local vulnerability and global connectivity jointly shape neurodegenerative disease propagation," *PLoS Biol*, vol. 17, no. 11, p. e3000495, 2019.

[4] M. Bertsch, B. Franchi, N. Marcello, M. C. Tesi, and A. Tosin, "Alzheimer's disease: a mathematical model for onset and progression," *Mathematical Medicine and Biology*, p. dqw003, 2016.

[5] J. Weickenmeier, E. Kuhl, and A. Goriely, "Multiphysics of prionlike diseases: Progression and atrophy," *Physical review letters*, vol. 121, no. 15, p. 158101, 2018.

[6] J. Weickenmeier, M. Jucker, A. Goriely, and E. Kuhl, "A physics-based model explains the prion-like features of neurodegeneration in alzheimer's disease, parkinson's disease, and amyotrophic lateral sclerosis," *Journal of the Mechanics and Physics of Solids*, vol. 124, pp. 264–281, 2019.

[7] A. Raj, A. Kuceyeski, and M. Weiner, "A network diffusion model of disease progression in dementia," *Neuron*, vol. 73, no. 6, pp. 1204–1215, 2012.

[8] A. Raj, E. LoCastro, A. Kuceyeski, D. Tosun, N. Relkin, M. Weiner, A. D. N. I. (ADNI, and others), "Network diffusion model of progression predicts longitudinal patterns of atrophy and metabolism in alzheimer's disease," *Cell reports*, vol. 10, no. 3, pp. 359–369, 2015.

[9] F. Abdelnour, H. Voss, and A. Raj, "Network diffusion accurately models the relationship between structural and functional brain connectivity networks," *Neuroimage*, vol. 90, pp. 335–347, 2014.

[10] S. Pandya, C. Mezias, and A. Raj, "Predictive model of spread of progressive supranuclear palsy using directional network diffusion," *Frontiers in neurology*, vol. 8, p. 692, 2017.

[11] G. R. Poudel, I. H. Harding, G. F. Egan, and N. Georgiou-Karistianis, "Network spread determines severity of degeneration and disconnection in huntington's disease," *Human brain mapping*, 2019.

[12] F. S., S. A., G. A., and E. Kuhl, "Prion-like spreading of alzheimer's disease within the brain's connectome," *Interface R. Society*, 2019.

[13] ——, "Spatially-extended nucleation-aggregation-fragmentation models for the dynamics of prion-like neurodegenerative protein-spreading in the brain and its connectome," *J. Theor. Biol.*, 2019.

[14] T. Thompson, P. Chaggar, E. Kuhl, and A. Goriely, "Protein-protein interactions in neurodegenerative diseases: a conspiracy theory," *bioRxiv*, 2020.

[15] H. Braak and E. Braak, "Neuropathological stageing of alzheimer-related changes," *Acta neuropathologica*, vol. 82, no. 4, pp. 239–259, 1991.

[16] H. Braak, I. Alafuzoff, T. Arzberger, H. Kretzschmar, and K. Del Tredici, "Staging of alzhimer disease-associated neurofibrillary pathology using paraffin sections and immunocytochemistry," *Acta Neuropathol*, vol. 112, no. 4, pp. 389–404, 2006.

[17] S. L. DeVos, B. T. Corjuc, D. H. Oakley, C. K. Nobuhara, R. N. Bannon, A. Chase, C. Commins, J. A. Gonzalez, P. M. Dooley, M. P. Frosch *et al.*, "Synaptic tau seeding precedes tau pathology in human alzheimer's disease brain," *Frontiers in neuroscience*, vol. 12, p. 267, 2018.

[18] M. Jucker and L. C. Walker, "Propagation and spread of pathogenic protein assemblies in neurodegenerative diseases," *Nature neuroscience*, vol. 21, no. 10, pp. 1341–1349, 2018.

[19] T. T. Olsson, O. Klementieva, and G. K. Gouras, "Prion-like seeding and nucleation of intracellular amyloid-β," *Neurobiology of disease*, vol. 113, pp. 1–10, 2018.

[20] M. Jucker and L. C. Walker, "Self-propagation of pathogenic protein aggregates in neurodegenerative diseases," *Nature*, vol. 501, no. 7465, pp. 45–51, 2013.

[21] F. Clavaguera, I. Lavenir, B. Falcon, S. Frank, M. Goedert, and M. Tolnay, ""prion-like" templated misfolding in tauopathies," *Brain pathology*, vol. 23, no. 3, pp. 342–349, 2013.

[22] M. Goedert, "Alzheimer's and parkinson's diseases: The prion concept in relation to assembled aβ, tau, and α-synuclein," *Science*, vol. 349, no. 6248, p. 1255555, 2015.

[23] A. Mudher, M. Colin, S. Dujardin, M. Medina, I. Dewachter, S. M. A. Naini, E.-M. Mandelkow, E. Mandelkow, L. Buée, M. Goedert *et al.*, "What is the evidence that tau pathology spreads through prion-like propagation?" *Acta neuropathologica communications*, vol. 5, no. 1, p. 99, 2017.

[24] R. M. Nisbet, J.-C. Polanco, L. M. Ittner, and J. Götz, "Tau aggregation and its interplay with amyloid-β," *Acta neuropathologica*, vol. 129, no. 2, pp. 207–220, 2015.

[25] D. Selkoe, "Alzheimer's disease is a synaptic failure," *Science*, vol. 298, pp. 789–791, 2002.

[26] M. A. Busche, S. Wegmann, S. Dujardin, C. Commins, J. Schiantarelli, N. Klickstein, T. V. Kamath, G. A. Carlson, I. Nelken, and B. T. Hyman, "Tau impairs neural circuits, dominating amyloid-β effects, in alzheimer models in vivo," *Threshold*, vol. 30, no. 40, p. 50, 2019.

[27] H. Cho, J. Y. Choi, M. S. Hwang, Y. J. Kim, H. M. Lee, H. S. Lee, J. H. Lee, Y. H. Ryu, M. S. Lee, and C. H. Lyoo, "In vivo cortical spreading pattern of tau and amyloid in the alzheimer disease spectrum," *Annals of neurology*, vol. 80, no. 2, pp. 247–258, 2016.

[28] C. R. Jack, D. A. Bennett, K. Blennow, M. C. Carrillo, B. Dunn, S. B. Haeberlein, D. M. Holtzman, W. Jagust, F. Jessen, J. Karlawish *et al.*, "Nia-aa research framework: Toward a biological definition of alzheimer's disease," *Alzheimer's & Dementia*, vol. 14, no. 4, pp. 535–562, 2018.

[29] R. E. Bennett, A. B. Robbins, M. Hu, X. Cao, R. A. Betensky, T. Clark, S. Das, and B. T. Hyman, "Tau induces blood vessel abnormalities and angiogenesis-related gene expression in p301l transgenic mice and human alzheimer's disease," *Proceedings of the National Academy of Sciences*, vol. 115, no. 6, pp. E1289–E1298, 2018.

[30] R. E. Bennett, S. L. DeVos, S. Dujardin, B. Corjuc, R. Gor, J. Gonzalez, A. D. Roe, M. P. Frosch, R. Pitstick, G. A. Carlson *et al.*, "Enhanced tau aggregation in the presence of amyloid β," *The American journal of pathology*, vol. 187, no. 7, pp. 1601–1612, 2017.

[31] L. M. Ittner and J. Götz, "Amyloid-β and tau—a toxic pas de deux in alzheimer's disease," *Nature Reviews Neuroscience*, vol. 12, no. 2, p. 67, 2011.

[32] A. M. Pooler and B. T. e. a. Hyman, "Amyloid accelerates tau propagation and toxicity in a model of early alzheimer's disease," *Acta Neuropathologica Communications*, vol. 3, no. 1, p. 14, 2015. [Online]. Available: https://doi.org/10.1186/s40478-015-0199-x

[33] A. Delacourte, J.-P. David, N. Sergeant, L. Buee, A. Wattez, P. Vermersch, F. Ghozali, C. Fallet-Bianco, F. Pasquier, F. Lebert *et al.*, "The biochemical pathway of neurofibrillary degeneration in aging and alzheimer's disease," *Neurology*, vol. 52, no. 6, pp. 1158–1158, 1999.

[34] K. Friston, "Functional and Effective Connectivity: A Review," *Brain Connect.*, vol. 1, no. 1, pp. 13–36, 2011.

[35] Y. Shi and A. Toga, "Connectome imaging for mapping human brain pathways," *Mol. Psychiatry*, vol. 22, pp. 1230–1240, 2017.

[36] E. Bullmore and D. Bassett, "Brain graphs: graphical models of the human brain connectome," *Annu. Rev. Clin. Psychol.*, vol. 7, pp. 113–140, 2011.

[37] A. Daducci, S. Gerhard, and J.-P. e. a. Thiran, "The Connectome Mapper: An Open-Source Processing Pipeline to Map Connectomes with MRI," *PLoS One*, vol. 7, no. 12, p. e48121, 2012.

[38] B. Jeurissen, M. Descoteaux, S. Mori, and A. Leemans, "Diffusion MRI fiber tractography of the brain," *NMR Biomed.*, vol. 4, no. 32, p. e3785, 2019.

[39] C. Kerepesi, B. Szalkai, and B. e. a. Varga, "The braingraph.org database of high resolution structural connectomes and the brain graph tools," *Cogn. Neurodyn.*, vol. 11, pp. 483–486, 2017.

[40] J.-D. Tournier, F. Calamante, and A. Connelly, "MRtrix: Diffusion tractography in crossing fiber regions," *Int. J. Imaging Syst. Technol.*, vol. 22, no. 1, pp. 53–66, 2012.

[41] J. Vogel, Y. Iturria-Medina, O. Strandberg, R. Smith, E. Levitis, A. Evans, and O. Hansson, "Spread of pathological tau proteins through communicating neurons in human alzheimer's disease," *Nat. Commun.*, vol. 11, no. 2612, 2020.

[42] P. Kevrekidis, T. Thompson, and A. Goriely, "Anisotropic Diffusion and Traveling Waves of Toxic Proteins in Neurodegenerative Diseases," *arXiv:2007.02421*, 2020.

[43] M. X. Henderson, S. Sedor, I. McGeary, E. J. Cornblath, C. Peng, D. M. Riddle, H. L. Li, B. Zhang, H. J. Brown, M. F. Olufemi *et al.*, "Glucocerebrosidase activity modulates neuronal susceptibility to pathological α-synuclein insult," *Neuron*, 2019.

[44] A. Goriely, E. Kuhl, and C. Bick, "Neuronal oscillations on evolving networks: dynamics, damage, degradation, decline, dementia, and death," *Physical review letters*, vol. 125, no. 12, p. 128102, 2020.

[45] E. Toro and A. Hidalgo, "ADER finite volume schemes for nonlinear reaction–diffusion equations," *Appl. Numer. Math.*, vol. 59, no. 1, pp. 73–100, 2009.

[46] R. Hosek and J. Volek, "Discrete advection–diffusion equations on graphs: Maximum principle and finite volumes," *Appl. Math. Comput.*, vol. 361, no. 15, pp. 630–644, 2019.

[47] L. O'Donnell and C.-F. Westin, "An introduction to diffusion tensor image analysis," *Neurosurg. Clin. N. Am.*, vol. 2, no. 22, pp. 185–viii, 2011.

[48] T. Sarwar, K. Ramamohanarao, and A. Zalesky, "Mapping connectomes with diffusion MRI: deterministic or probabilistic tractography?" *Magn. Reson. Med.*, vol. 81, no. 2, pp. 1368–1384, 2019.

[49] C.-H. Yeh, R. Smith, T. Dhollander, F. Calamante, and A. Connelly, "Connectomes from streamlines tractography: Assigning streamlines to brain parcellations is not trivial but highly consequential," *Neuroimage*, vol. 199, pp. 160–171, 2019.

[50] S. Pandya, Y. Zeighami, B. Freeze, M. Dadar, D. Collins, and A. Raj, "Predictive model of spread of Parkinson's pathology using network diffusion," *NeuroImage*, vol. 192, pp. 178–194, 2019.

[51] P. Winklewski, A. Sabisz, P. Naumczyk, K. Jodzio, E. Szurowska, and A. Szarmach, "Understanding the Physiopathology Behind Axial and Radial Diffusivity Changes—What Do We Know?" *Front. Neurol.*, vol. 9, no. 92, pp. 1–6, 2018.

[52] T. Thompson, G. Meisl, and A. Goriely, "The role of clearance mechanisms in the kinetics of toxic protein aggregates involved in neurodegenerative diseases," *arXiv:2009.14135*, pp. 1–25, 2020.

[53] G. Meisl, K. Zuo, T. Knowles, and D. e. a. Klenerman, *bioRxiv*.

[54] A. Schäfer, E. Mormino, and E. Kuhl, "Network Diffusion Modeling Explains Longitudinal Tau PET Data," *Front. Neurosci.*, vol. 14, p. 1370, 2020.